A self-powered surface sensing approach for detection of bottom-up cracking in asphalt concrete pavements: Theoretical/numerical modeling

Article *in* Construction and Building Materials · July 2017

DOI: 10.1016/j.conbuildmat.2017.03.197

CITATIONS
25

READS
496

4 authors, including:

Hassene Hasni
Michigan State University
35 PUBLICATIONS **532** CITATIONS
SEE PROFILE

Amir H. Alavi
University of Pittsburgh
208 PUBLICATIONS **10,800** CITATIONS
SEE PROFILE

Karim Chatti
Michigan State University
122 PUBLICATIONS **1,161** CITATIONS
SEE PROFILE

A Self-Powered Surface Sensing Approach for Detection of Bottom-Up Cracking in Asphalt Concrete Pavements: Theoretical/Numerical Modeling

Hassene Hasni, Amir H. Alavi*, Karim Chatti, Nizar Lajnef

Department of Civil and Environmental Engineering, Michigan State University, East Lansing, MI 48824, USA

Abstract

This study presents a self-powered surface sensing approach for detection of bottom-up cracking in asphalt concrete (AC) pavements. The proposed method was based on the interpretation of compressed data stored in memory cells of a self-powered wireless sensor (SWS) with non-constant injection rates. Different 3D finite element (FE) models of an AC pavement were developed using ABAQUS to generate the sensor output data. A realistic dynamic moving load was applied to the surface of the pavement via DLOAD subroutines developed by FORTRAN. A network of sensing nodes was placed at the top of the AC layer to assess their sensitivity to the progression of bottom-up cracks. Several damage states were defined using Element Weakening Method (EWM). A linear-viscoelastic behavior was considered for the AC layer. In order to detect the damage progression, several damage indicator features were extracted from the data acquisition nodes. The damage detection accuracy was improved through a data fusion model that included the effect of group of sensors. The proposed fusion model was based on the integration of a Gaussian mixture model (GMM) for defining descriptive features, different feature selection algorithms, and a robust computational intelligence approach for multi-class damage classification. Furthermore, an uncertainty analysis was carried out to verify the

*Corresponding Author: Amir Alavi
E-mail: alavi@msu.edu, ah_alavi@hotmail.com (A.H. Alavi)

reliability of the proposed damage detection approach. The results indicate that the progression of the bottom-up cracks can be accurately detected using the developed intelligent self-powered surface sensing system.

Keywords: Pavement health monitoring; Self-powered wireless sensor; Finite element modeling; Moving load; Data Fusion; Damage detection; Computational intelligence.

1. Introduction

Structures health monitoring (SHM) is focused on detection of damage in structures at early stages using advanced technologies. Pavement health monitoring is an extension of the SHM concept that deals with assessing the structural state of pavement infrastructure systems. Distresses concentrated in asphalt concrete (AC) layer can lead to the failure of the pavement structure over time. The maximum tensile stresses are commonly developed at the bottom of the AC layer under repetitive loadings. As a result, cracks usually initiate at the bottom of the asphalt layer and start propagating to the surface of the pavement. This so-called bottom-up fatigue cracking is one of the main failure modes in asphalt pavements. The fatigue life of pavements is mainly related to the nature and the amplitude of the applied loading. A dynamic analysis and a realistic loading modeling are essential to provide accurate prediction of the pavement response. However, most of traditional pavement analysis methods assume a uniform circular loading area and a stationary analysis. Previous studies show that these assumptions may result in an unrealistic pavement response [1, 2]. Dynamic loading may increase the fatigue damage by a factor between 2 to 7 [1]. Under the dynamic wheel effect, rutting damage may reduce the service life of the pavement by at least 40% [2].

Furthermore, Yoo and Al-Qadi [2] showed that the dynamic pavement response is usually higher than a quasi-static analysis. In fact, the pavement dynamic response is essentially a function of the structure natural frequency as well as the external loading frequency. Yoo and Al-Qadi [2] concluded that there is about 39 % difference on the tensile strain at the bottom of the asphalt layer between a static and transient dynamic analysis. Gillespie et al. [3] argued that a truck speed of 36 mph has a loading frequency of about 4.6 Hz, and 6.5 Hz for 51 mph. Lourens [4] reported that the magnitude of the stress and deflections in pavement highly depends on the loading frequency and they are different from the results given by a static loading. Since 1940s, flexible pavements are usually modeled as a linear elastic multilayer system based on the theory of the two-layered elastic systems developed by Burmister in 1943. However, hot-mix asphalt (HMA) behaves as a viscoelastic material. This type of material exhibits time-, rate- and temperature-dependent behavior. Al-Qadi et al. [5] and Elseifi et al. [6] showed that the approximation of multilayered linear elastic system underestimates the pavement responses at high temperatures or under a slow moving load. Furthermore, the HMA mixture behaves as an elastic material only at low temperatures and high loading frequencies. Therefore, an efficient pavement modeling should consider both the variation of the loading in time and space, the material on frequency and temperature and the amplitude of the applied stress.

From a sensing perspective, strain gages are widely used in roadways to detect variations in strains associated with pavement deterioration [7-10]. However, the installation of many of the existing sensors demands considerable care during construction. The commonly-used H-shaped strain gages require precise individual placement and wiring systems. To cope with these limitations, recent development in the field of pavement health monitoring has revealed the capabilities of wireless sensors networks (WSN) [11-18]. However, nearly all of the available

wireless sensors need an external power supply to activate the sensor. As a consequence, periodic replacement of the sensor battery is needed. This becomes more challenging and sometimes impractical for the long-term pavement health monitoring. Therefore, energy harvesting methods have been used for the empowering of the sensors [15, 19]. One of the most efficient energy harvesting methods is the use of piezoelectric transducers. This family of material has the ability of converting the mechanical energy into an electrical charge by harvesting the micro-strain energy from structure. Thereafter, by embedding a network of the piezoelectric transducers inside the asphalt pavement layer, they can generate electricity needed to empower the sensor. In this context, a self-powered wireless sensor (SWS) has been developed at Michigan State University (MSU) based on the "smart" pebble concept [10, 20, 21]. There are very few studies on the applicability of this sensor for SHM [10, 15]. In the pavement health monitoring area, Lajnef et al. [10] showed that the pavement fatigue life can be predicted using the SWS. Alavi et al. [14] have tested the ability of the sensor in detecting and localizing bottom-up cracks in asphalt pavement using the SWS with constant injection rate. They embedded the sensor inside the AC layer using a spherical epoxy packaging. The sensing system was placed two inches far from the bottom of the layer. Finite element (FE) simulations were performed to assess the strain amplitude changes due to bottom-up cracking [14]. The developed FE models were based on an elastic material behavior and a quasi-static loading. Moreover, Alavi et al. [14] showed that only the sensors located above the crack experience a notable change due to damage growth. However, a disadvantage of embedding the sensors at the bottom of the AC layer is that they may be damaged due to excessive stresses. Furthermore, new pavement construction projects are negligible when compared to the extent of the exiting pavement network. It is thus more critical for State Highway Agencies (SHAs) to adopt

monitoring techniques that can be adapted to existing pavements. It should be noted that surface sensing technologies such as remote sensing are commonly used for the monitoring of existing pavements. These methods use the electromagnetic spectrum to identify the surface and subsurface defects. In this context, ground-penetrating radar (GPR) employs the electromagnetic energy to detect subsurface anomalies. GPR can be used for both measuring the pavement thickness and locating voids. GPRs are able to identify cracks and measure cracks depth between 50 to 160 mm in flexible pavements. They can be attached to a service vehicle travelling at highway speed [22]. However, major limitations of such methods are that they need notable energy to operate and may not be practical for continuous long-term monitoring purposes.

In order to cope with the limitations of the existing monitoring methods, this study proposes a self-powered wireless surface sensing approach for the detection of bottom-up cracking in existing asphalt pavements. The proposed method would not have major interference with regular pavement maintenance activities. The SWSs can have floating-gates with constant injection and non-constant injection rates. The previous research conducted by our team has been focused on the SWS with non-constant injection rate [14-18]. While the working principal is the same, the difference between the two classes of sensors is in the form of data outputted from the sensors. Herein, the non-constant injection rate sensor was used. A dynamic analysis of a moving truck at highway speed was carried out through a realistic FE modeling. Different damage scenarios were considered by changing the size of the damage zone and the AC material properties. The sensor output was modeled based on the strains extracted from the surface of the AC layer at different sensing nodes. The sensors locations were defined in the longitudinal and transverse directions. Thereafter, features were extracted from the sensor data and fused to define

new set of explanatory features. Finally, a probabilistic neural network (PNN) classifier was used to classify the predefined damage scenarios.

2. Finite element modeling of pavement structure subjected to a moving load

2.1. Geometry and FE model

ABAQUS software was employed to simulate the response of the pavement under a moving load. In the FE analysis, the stress/strain response is sensitive to the element type and size as well as the boundary conditions. In this study, 3D FE models were developed as they are more appropriate compared to a 2D axisymmetric model. In fact, a 3D model allows simulating the contact stresses between the tire footprint and the pavement surface. The pavement model was meshed using two different types of elements: eight-node linear brick elements with reduced integration (C3D8R) and eight node linear infinite elements (CIN3D8). The standard finite elements were used to model the region of interest and the infinite elements were deployed in the far field region. This type of elements allows providing silent boundaries to the FE model in the dynamic analysis and reduces the number of elements at far field [23]. These elements have a special shape function to vanish the displacement field when the coordinates approach infinity. Such boundary type can minimize the reflection of the shear and dilatational waves back into the FE mesh [24, 25]. In a dynamic analysis, the infinite elements introduce additional normal and shear tractions on the FE boundary using a viscos damping boundary. The introduced normal and shear stresses are proportional to the velocity components as follows [25]:

$$\sigma = \rho\, c_p \dot{u} \tag{1}$$

$$\tau = \rho\, c_s \dot{v} \tag{2}$$

where $\rho, \sigma, \tau, c_p, c_s, \dot{u}$ and $\dot{v}$ are the material density, normal stress along the interface between the FE/infinite elements, shear stress along the interface FE/infinite elements, longitudinal wave velocity, shear wave velocity, normal velocity and tangential velocity, respectively. The wave velocities are given by the following expressions [25]:

$$c_p = \sqrt{\frac{(1-\nu)E}{(1-2\nu)(1+\nu)\rho}} \tag{3}$$

$$c_s = \sqrt{\frac{E}{2(1+\nu)\rho}} \tag{4}$$

where E and ν are the Young modulus and Poisson's ratio, respectively. In this study, the length of the pavement section was 7 meters in the longitudinal direction (parallel to the traffic direction) and 6 meters in the transverse direction (perpendicular to the traffic direction). The pavement thickness was 6.3 meter. The pavement was composed of three layers: AC, base and subgrade layers. The thickness of the AC, base and subgrade layers are 100 mm, 200 mm and 6000 mm, respectively. Large model dimensions were used to reduce the edge effect and to achieve a full passage of the tire on the pavement section. Fig. 1 displays the pavement model as well as the meshed cross section of the AC layer. According to a study conducted by Duncan et al. [26], the location of the infinite elements should be at least 12 times the radius of the loading area (R) in the horizontal direction. In this paper, the infinite domain was located at approximately 16R from the initial and final locations of the load center in the longitudinal direction, and 17R in the transverse direction. The total number of elements was 393,796, from which 363,440 elements are C3D8R and 30,356 elements are CIN3D8. Fig. 2 displays the structure of CIN3D8. A fine mesh was used around the loading path and a coarse mesh far away from the load. Different simulations were conducted to study the effect of the element

dimensions on the pavement response. It was found that an element with dimensions of 20 mm × 20 mm could accurately capture the stress/strain response under the wheel footprint.

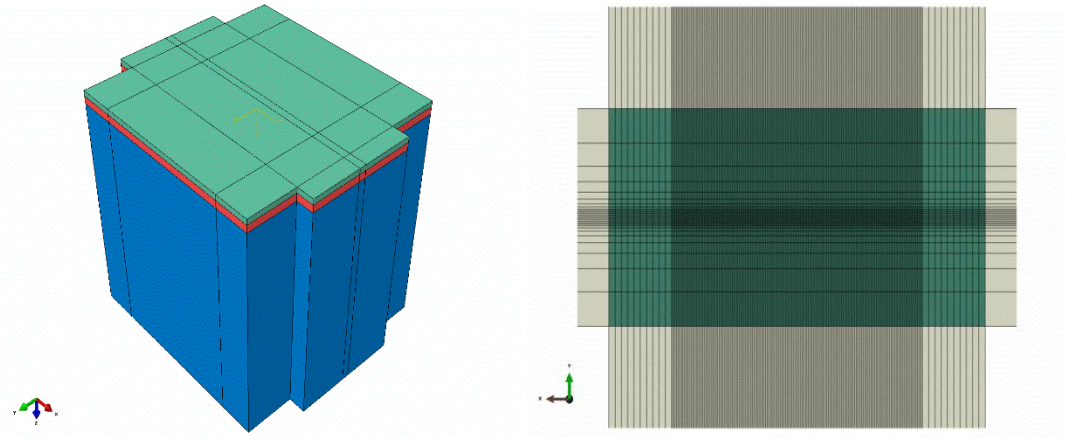

(a) (b)

Fig. 1. (a) The 3D FE model of the pavement structure, **(b)** Meshed cross section of the AC layer.

The element thickness was chosen to be 10 mm for the AC layer, 20 mm for the base and from 20 mm to 500 mm for the subgrade. Furthermore, in a dynamic analysis, it is recommended that the maximum element size should not exceed 1/12 the minimum length of the elastic waves propagating inside the structure [25].

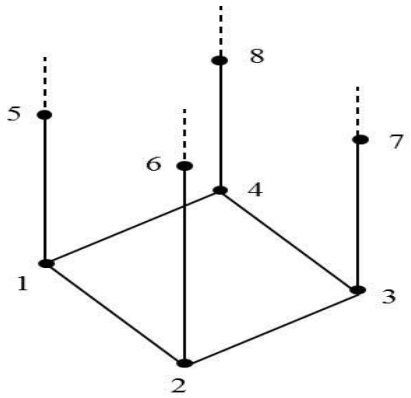

Fig. 2. CIN3D8 element structure.

The natural frequency of a typical flexible pavement, the vehicle loading frequency and the stress wave velocity are around 6-14 Hz, 0.1-25 Hz and 100 m/s to 600 m/s, respectively [25]. Accordingly, the defined element size is small enough to satisfy the minimum element size requirement.

2.2. Dynamic analysis

For pavement analysis, the loading can be modeled as a static, quasi-static or dynamic loading. If the loading is stationary, a static analysis is suitable for the analysis. A quasi-static approach is a sequence of static loads that are moving from one position to another at each time step. Static and quasi-static analyses do not include the effect of inertia forces. However, a dynamic analysis is more appropriate if the load is moving with a certain speed in which the loading changes in time and location according to the truck speed. Therefore, this type of analysis was used in this study. The moving load problem can be treated as structural dynamic problem as it considers slower load changes than wave propagation problems. The response in a wave propagation problem is rich in high frequency mode shapes. The analysis time is also in the order of the wave travel time across the structure. Therefore, a very short time step is required for this type of analysis. In a structural dynamic problem, the response is dominated by low modes and the effect of high modes is insignificant [27, 28]. If the time required for the stress waves to propagate through the whole structure does not exceed a small portion of the load rise duration, the problem can be assumed to be a structural dynamic problem. As the vehicle speed is much smaller than the stress wave speed (100 m/s to 600 m/s), the problem was treated as a structural dynamic problem in this study. The equation of motion of a multi-degree of freedom system is as given below:

$$M\,\ddot{u} + C\,\dot{u} + K\,u = F \tag{5}$$

where M is the mass matrix, C is the damping matrix, K is the stiffness matrix, u is the displacement vector and F is the external force vector. The first term of the equation $M\,\ddot{u}$ represents the inertia forces and $(C\,\dot{u} + K\,u)$ represents the internal forces.

There are two ways to solve this type of nonlinear equations; an implicit direct integration or an explicit direct integration method. The implicit procedure is more suitable for structural dynamic problems and usually provides good numerical stability. For the method, the displacements at two consecutive times are calculated by solving a set of nonlinear equations simultaneously.

In a dynamic analysis, the selection of the time increment is very important. According to Bathe, the time increment Δt should be less than or equal to $\frac{1}{20\,f_{dominant}}$ [28]:

$$\Delta t \leq \frac{1}{20\,f_{dominant}} \tag{6}$$

where $f_{dominant}$ is dominant frequency of the response of the structure or of the loading. Herein, the time increment was taken 0.001 s which satisfies the time increment requirement as the highest loading frequency is usually lower than 10 Hz.

2.3. Material characterization

Each layer of the modeled pavement had unique material properties. The HMA layer had viscoelastic properties while an elastic behavior was considered for the base and subgrade layers. The HMA modulus is time (frequency) and temperature dependent. In fact, the state of the stress in the AC layer does not only depend on the current strain but on the entire strain history. The expression of the stress in linear viscoelasticity can be expressed by a Boltzmann superposition integral as follows [29]:

$$\sigma(t) = \int_0^t E(t - \tau)\frac{d\varepsilon}{d\tau}\,d\tau \tag{7}$$

In the present study, a generalized Maxwell model was used for representing the linear-viscoelastic behavior of the HMA. This model is a combination of Maxwell elements (one spring and one dashpot) connected in parallel with a spring as shown in Fig 3.

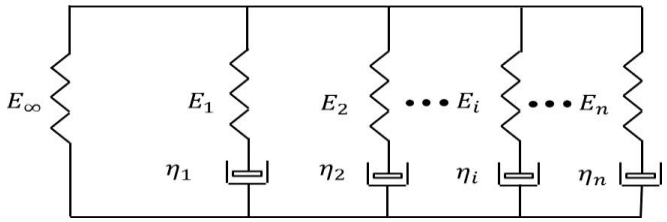

Fig. 3. Generalized Maxwell model consisting of n Maxwell elements connected in parallel.

A single element Maxwell model is composed of one spring and one dashpot mounted in series. Therefore, the relationship between the stress-strain is expressed as follows [29]:

$$\dot{\varepsilon}(t) = \frac{\dot{\sigma}(t)}{E} + \frac{\sigma(t)}{\eta} \tag{8}$$

where E is the elastic modulus and η is the viscosity parameter.

If the material is subjected to a constant strain ε_0, the solution of the precedent equation becomes:

$$\sigma(t) = E\varepsilon_0 \exp\left(-\frac{t}{\tau}\right) \text{ where } \tau = \frac{\eta}{E} \tag{9}$$

where τ represents the relaxation time. By performing a summation over the n Maxwell elements shown in Fig. 3, the stress equation becomes:

$$\sigma(t) = E_\infty\varepsilon_0 + \sum_{i=1}^{n} E_i\varepsilon_0 \exp\left(-\frac{t}{\tau_i}\right) = \left(E_\infty + \sum_{i=1}^{n} E_i \exp\left(-\frac{t}{\tau_i}\right)\right)\varepsilon_0 \tag{10}$$

Therefore, the relaxation modulus:

$$E(t) = \frac{\sigma(t)}{\varepsilon_0} = E_\infty + \sum_{i=1}^{n} E_i \exp\left(-\frac{t}{\tau_i}\right) \tag{11}$$

This expression is the Prony series representation. The equilibrium modulus is E_∞ and the instantaneous modulus E_0 is the value of E(t) at t =0 given by:

$$E_0 = E_\infty + \sum_{i=1}^{n} E_i \quad (12)$$

By replacing the equilibrium modulus E_∞ by $(E_0 - \sum_{i=1}^{n} E_i)$, Eq. (11) can be rewritten as follows:

$$E(t) = E_0 - \sum_{i=1}^{n} E_i \left(1 - \exp\left(-\frac{t}{\tau_i}\right)\right) \quad (13)$$

Therefore, the Prony series representation is fully defined by (E_i, τ_i). For the FE modeling, ABAQUS uses the dimensionless Prony series representation based on the shear (G) and bulk (K) moduli to define a viscoelastic behavior [29]:

$$G(t) = \frac{E(t)}{2\,(1+\nu)} \quad (14)$$

$$K(t) = \frac{E(t)}{3\,(1-2\nu)} \quad (15)$$

If we divide both expressions by the initial values G_0 and K_0 respectively, we obtain:

$$\bar{g}(t) = 1 - \sum_{i=1}^{n} \bar{g}_i \left(1 - \exp\left(-\frac{t}{\tau_i}\right)\right) \quad (16)$$

and

$$\bar{k}(t) = 1 - \sum_{i=1}^{n} \bar{k}_i \left(1 - \exp\left(-\frac{t}{\tau_i}\right)\right) \quad (17)$$

Therefore, there are three parameters required in order to define a viscoelastic material property in ABAQUS: the dimensionless shear relaxation modulus $\bar{g}_i$, the dimensionless bulk relaxation modulus $\bar{k}_i$, and the relaxation time τ_i. The relaxation modulus of the AC material used in this paper was defined by four constants c_i (i=1,2,3,4) from the sigmoid function given by the following expression:

$$Log(E(t)) = c_1 + \frac{c_2}{1+\exp(-c_3 - c_4 \log(t_r))} \quad (18)$$

where t_r is the reduced time and c_i are coefficients related to the type of the AC material. In this paper, the constants c_i were taken as follows:

- $C_1 = 0.639$
- $C_2 = 3.341$
- $C_3 = 0.709$
- $C_4 = -0.691$

A MATLAB code was developed to fit Eq. (11) to the relaxation modulus given by the sigmoid function (Eq. (18)) in order to obtain the Prony series coefficients. Fig. 4 displays the results of the Prony representation fit to the relaxation modulus. On this basis, 33 Prony coefficients were calculated. Thereafter, the dimensionless coefficients $\bar{g}_i$ and $\bar{k}_i$ were obtained based on the Prony coefficients E_i. The instantaneous modulus was calculated based on the equilibrium modulus and the 33 coefficients as expressed by Eq. (12):

$$E_0 = E_\infty + \sum_{i=1}^{33} E_i = 9548\ MPa \tag{19}$$

Table 1 presents the values used for the definition of the viscoelastic material property of the AC layer. The Poisson's ratio was equal to 0.35.

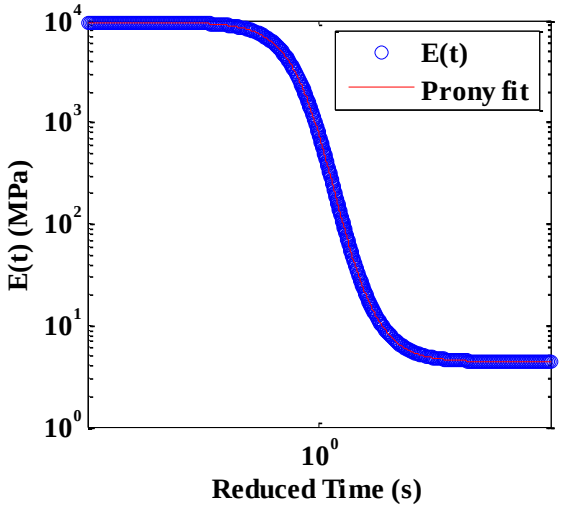

Fig. 4. Prony series fit to the relaxation modulus of the sigmoid function.

For the AC layer, there is no need to define an additional structural damping as it is behaves as a viscoelastic material. However, as the base and the subgrade are elastic materials, it is important to include an additional damping to include the effect of energy absorption when the wave propagates through the soil. Therefore, a 5 % damping ratio was defined for both the base and the subgrade layers. Table 2 presents the material properties of the three pavement layers.

Table 1. Prony series coefficients**.**

$\overline{g}_i$	$\overline{k}_i$	τ_i
0.000367	0.000367	1.00E-13
0.000262342	0.000262342	6.49E-13
0.000678368	0.000678368	4.22E-12
0.00108393	0.00108393	2.74E-11
0.00194552	0.00194552	1.78E-10
0.00338058	0.00338058	1.15E-09
0.00591073	0.00591073	7.50E-09
0.0102785	0.0102785	4.87E-08
0.0177787	0.0177787	3.16E-07
0.0304279	0.0304279	2.05E-06
0.0511115	0.0511115	1.33E-05
0.0829927	0.0829927	8.66E-05
0.126665	0.126665	0.000562
0.172722	0.172722	0.003652
0.193456	0.193456	0.023714
0.159339	0.159339	0.153993
0.0891806	0.0891806	1
0.0349519	0.0349519	6.49382
0.0112675	0.0112675	42.1697
0.00355265	0.00355265	273.842
0.00124161	0.00124161	1778.28
0.000492694	0.000492694	11547.8
0.000222137	0.000222137	74989.4
0.000108642	0.000108642	486968
5.68027e-05	5.68027e-05	3.16E+06
3.06136e-05	3.06136e-05	2.05E+07
1.69927e-05	1.69927e-05	1.33E+08
9.44883e-06	9.44883e-06	8.66E+08
5.45866e-06	5.45866e-06	5.62E+09
2.83722e-06	2.83722e-06	3.65E+10

2.16651e-06	2.16651e-06	2.37E+11
1.00153e-07	1.00153e-07	1.54E+12
1.83335e-06	1.83335e-06	1.00E+13

Table 2. Material properties.

Layer	Modulus (MPa)	Poisson's ratio	Density (Kg/m^3)	Damping (%)
HMA	9548	0.35	2325	-
Base	193	0.3	2000	5
Subgrade	43	0.4	1500	5

2.4. Loading

2.4.1. Contact area

Tire-pavement interaction is a complex phenomenon due to the tire footprint, non-uniform contact area, and shear stress components [30]. A tire footprint consists of many small surfaces contacting the pavement separated by ribs that may not make contact with pavement and thus may not contribute to the loading. Defining a tire footprint that simulates a real tire-pavement interaction is possible using the FE modeling. Tielking and Roberts [31] used the ILLIPAVE finite element pavement program to model non-uniform contact pressures of a tire moving on an asphalt pavement section. Their tire contact pressure model took into account normal pressure, transverse shear pressure, and longitudinal shear pressure. Their results showed that non-uniform tire contact pressure induced greater tensile strain at the bottom of the asphalt layer compared to uniform contact pressure. However, simplifying the tire contact pressure area can affect the pavement strain response since the distribution of the stress field in the contact zone is not uniform [31-33]. Tire pressure and load intensity affect contact stress distribution [31, 34-37]. In the multilayered elastic theory, the shape of the tire footprint is assumed to have a circular shape as it conserves the property of an axisymmetric problem. Wang and Machemehl [32] showed

that the assumption of a uniform circular tire-pavement pressure area can underestimate the compressive strains at the top of the subgrade and overestimate the tensile strains at the bottom of the AC layer. In most of the 3D FE modeling of pavements, the contact area between the tire and the pavement surface is approximated as a rectangle with two semi-circles as shown in Fig. 5. Previous studies showed that the shape of the contact area of a truck tire is more rectangular than circular [36]. Accordingly, in this paper, the contact area was assumed to be rectangular.

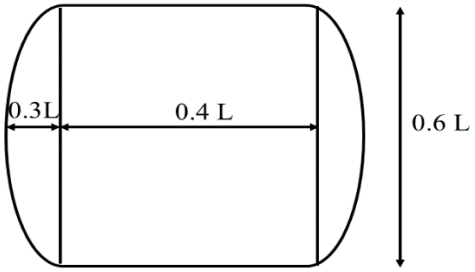

Fig. 5. Tire contact area.

The obtained contact area was transformed to a simple rectangle with the same width 0.6 L. The area of the contact area shown in Fig. 5 is equal to:

$$A_c = 0.4\,L \times 0.6\,L + 2 \times \left(\frac{\pi\,(0.3\,L)^2}{2}\right) = 0.5227\,L^2 \tag{20}$$

Therefore, if *a* denotes the length of the equivalent rectangle, the area of the equivalent rectangle (Fig.6) is:

$$A_c = a\ \times 0.6\,L = \ 0.5227\,L^2 \tag{21}$$

which gives: $a = \frac{0.5227\,L^2}{0.6\,L} = 0.8712\,L$

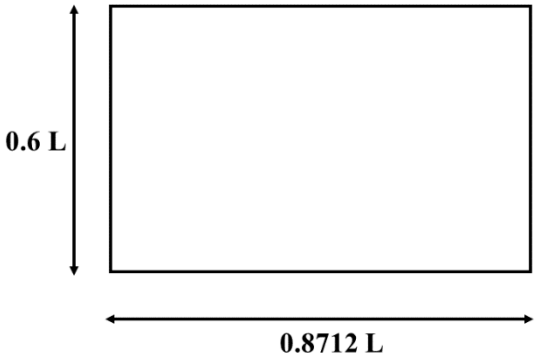

Fig. 6. Approximated rectangular loading.

The area of the contact area used in this paper is A_c = 0.0260 m^2. Therefore, L is given by:

$$L = \sqrt{\frac{A_c}{0.5227}} = \sqrt{\frac{0.0260}{0.5227}} = 0.2230\ m \tag{22}$$

Thus, the dimensions of the rectangle are: 0.8712 L = 0.1943 m and 0.6 L = 0.1338 m.

2.4.2. Contact pressure

The loading of the pavement occurred in the center strip of the section. Fig. 7 highlights the loaded strip. In order to simulate the movement of the load at the desired speed, a user defined DLOAD subroutine was developed using FORTRAN. In fact, regular loading functions in ABAQUS do not allow varying the location of the applied load as a function of time. In order to overcome this limitation, different approaches were proposed. The load and its amplitude can be shifted over the loading path at each step until a single wheel pass is completed [14, 38]. This approach is time consuming as it needs the definition of the footprint areas for each step. However, the DLOAD subroutine can be used to define the variation of the distributed load magnitude as function of the position, time, element number and load integration point number [23].

The script specifies the center of the rectangular loading area and its dimensions, the initial and final position of the truck, the truck speed and the tire pressure. A highway speed of 67 mph (30 m/s) was inputted to the FORTRAN code and a tire pressure of 862 kPa was applied. The location of the center of the contact area was calculated by the DLOAD subroutine in each time step as follows:

$$x = v_x \times t + x_0 \tag{23}$$

$$y = v_y \times t + y_0 \tag{24}$$

where v_x, v_y, x_0 and y_0 are the speed in x direction, the speed in the y direction, the x-coordinate of the initial location of the tire center and the y-coordinate of the initial location of the tire center. The vehicle speed was kept constant.

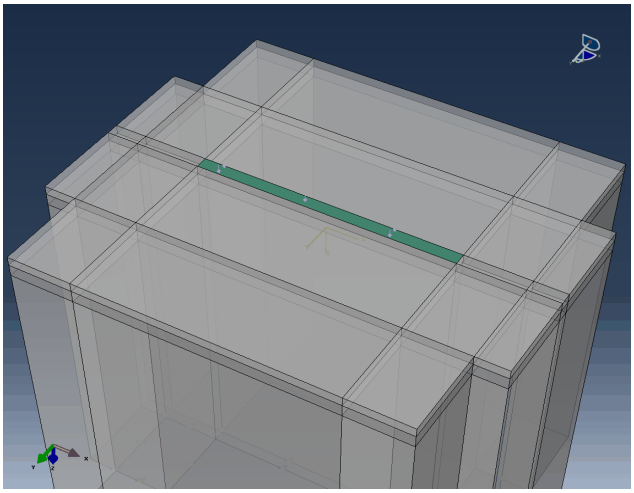

Fig.7. Loaded strip of the AC pavement section.

In this paper, the loading was assumed to follow the x-axis, therefore, $v_y$was set to zero. The chosen length of the loading path is 3 m. As the selected time step of the dynamic analysis was 0.001 second, the tire progresses by:

$$\Delta x_{time-step} = v\,\Delta t = 30 \times 0.001 = 0.03\,m = 30\,mm \tag{25}$$

As the size of the element around the loading path is 20mm × 20mm, only one element (in the longitudinal direction) was loaded in each time step.

2.5. Crack modeling

Many studies on fatigue of flexible pavements have been conducted using the FE software such as ABAQUS and FEP++ [35, 39-42]. These programs allow the user to define various complex parameters such as the viscoelastic properties of asphalt. A limitation of using the FE programs for asphalt pavement analysis pertains to the definition of highly complex scenarios such as fatigue cracking. Fatigue cracking can begin as either a bottom-up crack, top-down crack, or a combination of the two. After repeated loading, crack propagation and additional crack growth further weaken the pavement. These cracks that begin at one end can either continue growing through the thickness of the pavement or coalesce with a different crack growing in another direction. Modeling fatigue cracking inadequately can result in overestimating the fatigue life of the pavement [35]. Major factors affecting fatigue cracking are asphalt properties, asphalt thickness and tire pressure among others. Generally, top-down cracking increases in thicker asphalt layer, stiffer asphalt layer, less stiff base and/or subgrade and under non-uniform loading [35].

ABAQUS allows the user to define certain properties by user subroutines [23]. Detailed crack modeling is typically defined using a user subroutine in order to realize more realistic results due to limitations in the basic modeling methods. Cracks defined in ABAQUS using basic modeling for asphalt pavement yield inaccurate results due to over simplification of the crack. Modeling a crack in ABAQUS can be done using extended finite element method (XFEM). One major limitation that deters XFEM usage in the fatigue cracking of pavements is that the method is only

viable in static cases. Creating a user subroutine to accurately model complex fatigue cracking in asphalt has yet to be accomplished. Song et al. have developed a user subroutine of a cohesive fracture model that successfully replicated cracking in asphalt concrete [43]. Dave and Buttlar have successfully modeled thermal reflective cracking using a user-defined bilinear cohesive crack model [42]. A crack can also be introduced using Element Weakening Method (EWM). Mishnaevsky has used this method to simulate the reduced properties resulting from cracking of particle reinforced composites [44].

In this paper, the EWM was also used to introduce the damage to the pavement. Different scenarios were defined based on both the weakening state of elements defining the damage zone and the damage height. On this basis, the element elastic modulus was reduced to a certain value in order to define a damage state. A total of 13 damage states were studied which include 4 different cases of modulus reduction, each having three varying damage zone heights. A damage having a rectangular prismatic shape of 120 mm × 120 mm × damage height was created at the bottom center of the HMA layer. The modulus of this volume was reduced to 30%, 50%, 70% and 90% from the instantaneous modulus of the HMA layer. The damage zone heights were 20 mm, 40 mm and 60 mm. The defined damage states are given in Table 3. Fig. 8 shows the damage location, cross section and the measurement locations.

Table 3. Damage scenarios.

Damage state	Damage height (mm)	Reduction in the AC modulus (%)
Intact	0	0
D20W30	20	30
D20W50	20	50
D20W70	20	70
D20W90	20	90
D40W30	40	30
D40W50	40	50
D40W70	40	70
D40W90	40	90
D60W30	60	30
D60W50	60	50
D60W70	60	70
D60W90	60	90

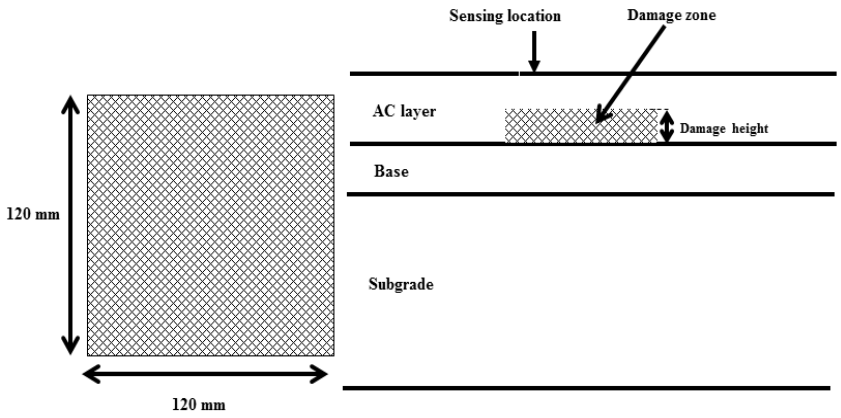

(a) (b)

Fig. 8. (a) Cross section of the damaged zone, **(b)** Damage zone and measurement location.

2.6. Sensors locations

Fig. 9 shows the location of the data acquisition nodes on the surface of the AC layer. A network of 32 elements was selected as the sensing nodes. The network was divided into 4 sets (Fig. 9). Each set contained 8 sensing nodes.

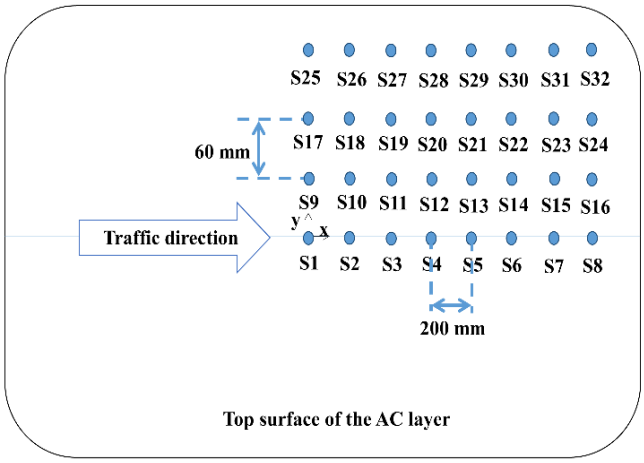

Fig. 9. Sensors locations.

The first sensor was located at x = 0 and the distance between two consecutive elements was 200 mm in the longitudinal direction. The transversal distance between two consecutive sets of sensors was 60 mm. Therefore, the offset of the sets from the center of the pavement (y = 0) was considered as follows:

- Set 1: y = 0
- Set 2: y = 60 mm
- Set 3: y = 120 mm
- Set 4: y = 180 mm

The longitudinal, transversal and principal strains for each of the predefined damage cases were subsequently extracted at the sensing nodes.

2.7. FE results

Fig. 10 shows the time history of the first principal strains (in absolute value) for different sensors and for the intact, D20W90, D40W90 and D60W90 damage states. As can be seen, for sensor S1, which is located above the damage zone, the amplitude of the strain increases with

damage growth. The difference of the amplitudes between the Intact and the D60W90 damage state is 111.7 $\mu\varepsilon$.

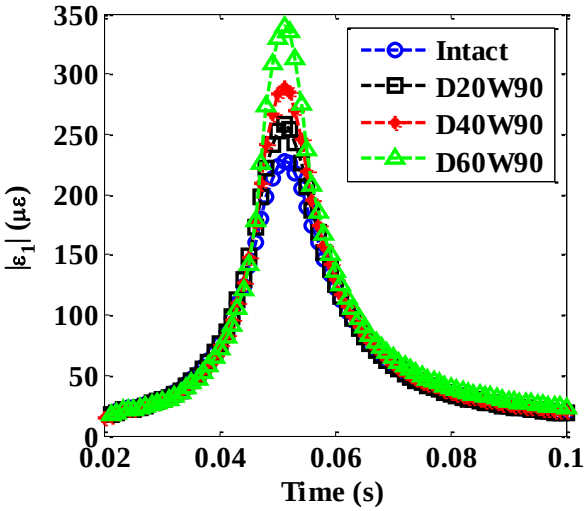

Fig. 10. Strain history of sensor S1 for different damage states.

Fig. 11 displays the results for sensor S2. Evidently, the difference between the maximum principle strains is being reduced comparing to sensor S1 as the sensor is located at a 200 mm offset from S1 (along the x-axis).

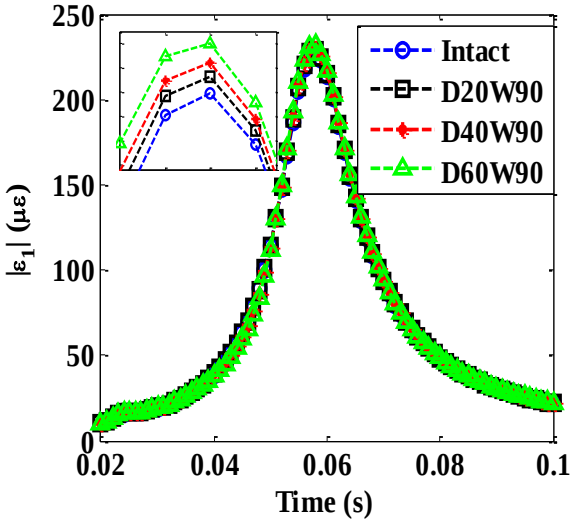

Fig. 11. Strain history of sensor S2 for different damage states.

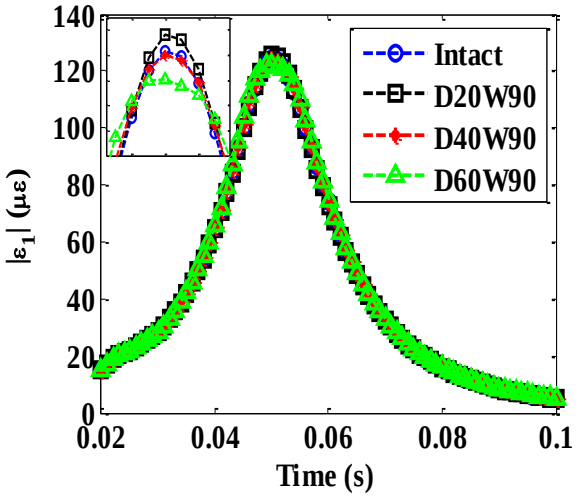

Fig. 12. Strain history of sensor S17 for different damage states.

Fig. 12 displays the results for sensor S17 which is located at x = 0 and at y = 120 mm. As seen can be seen in the figure, the amplitude of the strain is changing between damage states but it does not have an increasing trend as for sensors S1 and S2. However, for sensor S18, which has a 120 mm offset from the x-axis and 200 mm offset from the y-axis, the strain amplitude continuously increases as the damage progresses (Fig. 13). Based on the results, it can be concluded that the amplitude of the strains is affected by the damage progression as well as the location of the sensor with respect to the damage.

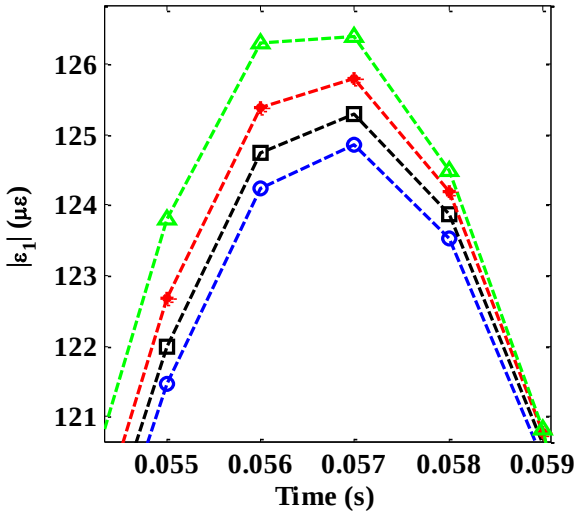

Fig. 13. Zooming around the peak values of sensor S18.

Fig. 14 presents the variation of the maximum first principal strain (in absolute value) with respect to the percentage of modulus reduction for different damage heights (h_d). As seen in these figures, the amplitude of the strain depends on the offset of the sensor with respect to the damage zone. In fact, for a fixed reduction in the asphalt modulus, the strain amplitude increases for sensors S1 and S2 but the behavior changes when the sensor is located at a certain offset from the damage center. Furthermore, as it is illustrated by sensor S17, for a fixed damage height, the strain increases with the percentage of modulus reduction for the case of 20 mm but it has a decreasing trend for the two other damage lengths (40 mm and 60 mm). However, when the sensors are located along the wheel path, a unique trend was observed. In this case, the amplitude of the first principal strain increases with the damage height and the percentage of modulus reduction.

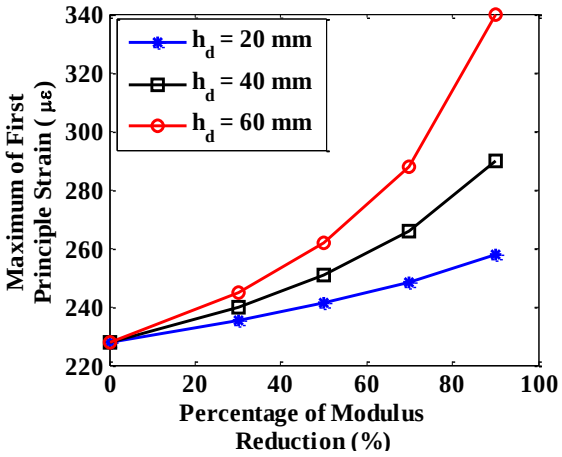

(a) Sensor S1

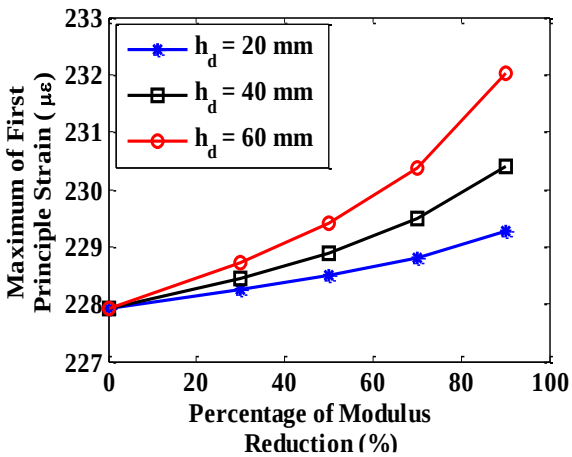

(b) Sensor S2

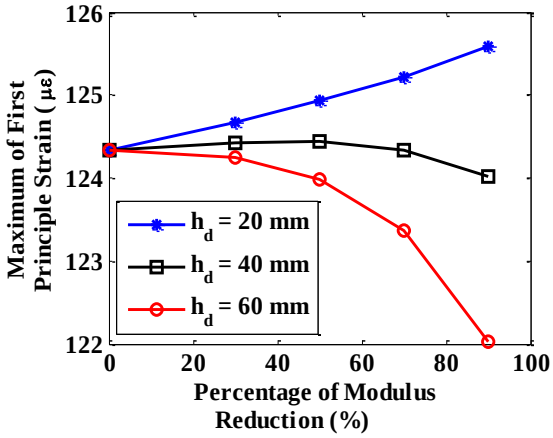

(c) Sensor S17

Fig. 14. Variation of the maximum principal strain with damage state.

3. The proposed damage detection approach using non-constant injection rate SWS

The damage detection approach proposed in this paper was divided into three stages. The first step was focused on generating and characterizing the sensor output based on the time history of the first principal strain obtained in the previous section. Thereafter, a feature transformation method was applied to the original set of data to find a sound relationship between the damage

progression and the data of the network of sensors. Finally, a PNN classifier was used to classify the pre-defined damage classes.

3.1. Working principle of a non-Constant injection rate SWS

The new class of SWS with non-constant injection rate memory cells (floating-gates) mainly works based on the strain-energy harvested from the structure under excitation using piezoelectric transducers. Fig. 15 shows a prototype of the SWS. The SWS has 7 memory cells that cumulatively store the droppage in strain at a predefined threshold level. Each cell has a specific threshold level and injection rate. When the amplitude of the strain at the sensor location exceeds the threshold level of a specific gate, it starts recording the cumulative strain droppage. The injection rate is defined as the quantity of droppage in strains in 1 second at a specific memory gates.

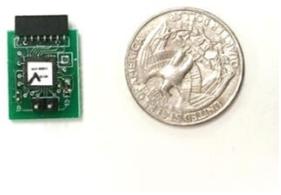

Fig. 15. Prototype of the SWS.

Fig. 16 displays the procedure of obtaining the strain droppage ($\varepsilon_0 - \varepsilon_{sensor}$) at the sensor level. As seen from the figure, the sensor strain droppage is in the form of a histogram that have different amplitudes for each gate. Each memory cell has an initial strain value ε_0. After applying a certain number of loading cycles, the initial strain decreases linearly with the number of cycles. Furthermore, the strain value ε_{sensor} at each gate could be written as:

$$\varepsilon_{sensor} = \varepsilon_0 - I_{gi} \sum_k \Delta t_k^{gi} \quad (26)$$

where I_{gi} is the of injection rate of gate g_i and Δt_k^{gi} is the k^{th} time intersection interval at gate g_i. In this paper, the case of a non-constant injection rate sensor was studied. In this case, the shape of the histogram is random and does not follow a specific trend. The injection rates play a very important role in characterizing the sensor output.

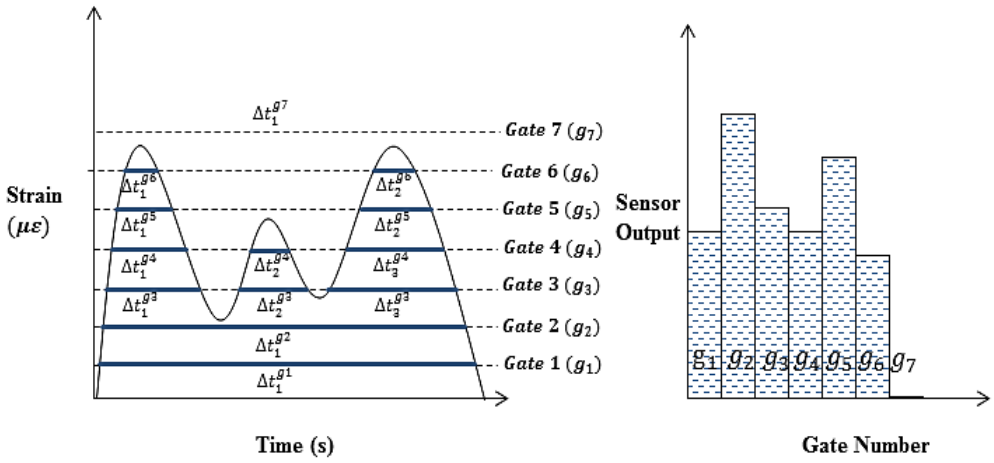

Fig. 16. Procedure of obtaining the sensor output.

For the analysis, the initial strain value in each memory was set to 500 $\mu\varepsilon$. The gate injection rates as well as the strain threshold levels are displayed in Table 4. The selection of the thresholds and injection rates was based on an existing sensor. The activation strain of the sensor is 80 $\mu\varepsilon$ below which the device does not record any information. The maximum threshold is 200 $\mu\varepsilon$.

Table 4. Preselected strain threshold levels and gates injection rates considered for the analysis.

Gate number	Strain threshold level ($\mu\varepsilon$)	Injection rates ($\mu\varepsilon/s$)
1	80	0.001000
2	100	0.005710
3	120	0.023162
4	140	0.027822
5	160	0.006562
6	180	0.005989
7	200	0.032792

Fig. 17 presents the variation of the sensor strain at each gate versus the number of applied cycles for the intact pavement and for one damage scenario. For brevity, only the results pertaining to the intact and D60W90 modes were compared for sensor S1.

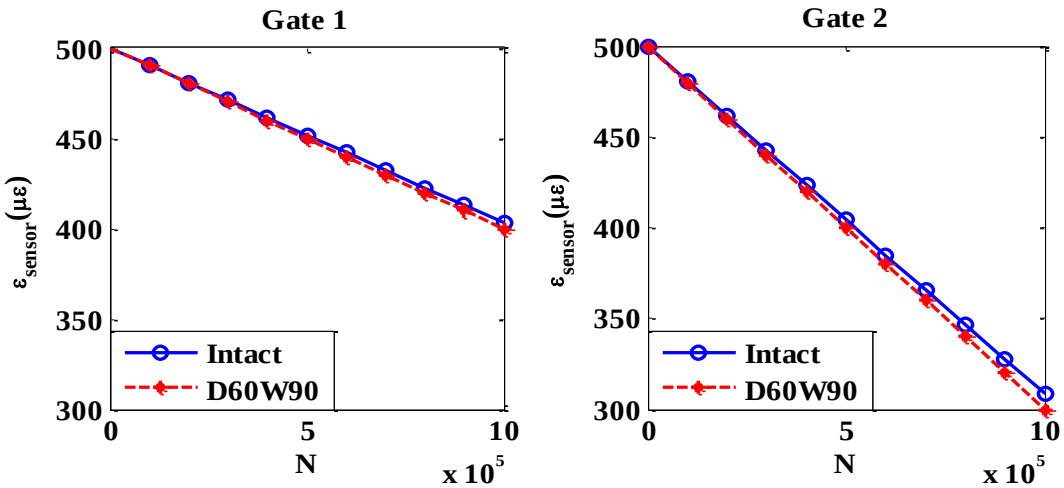

(a) (b)

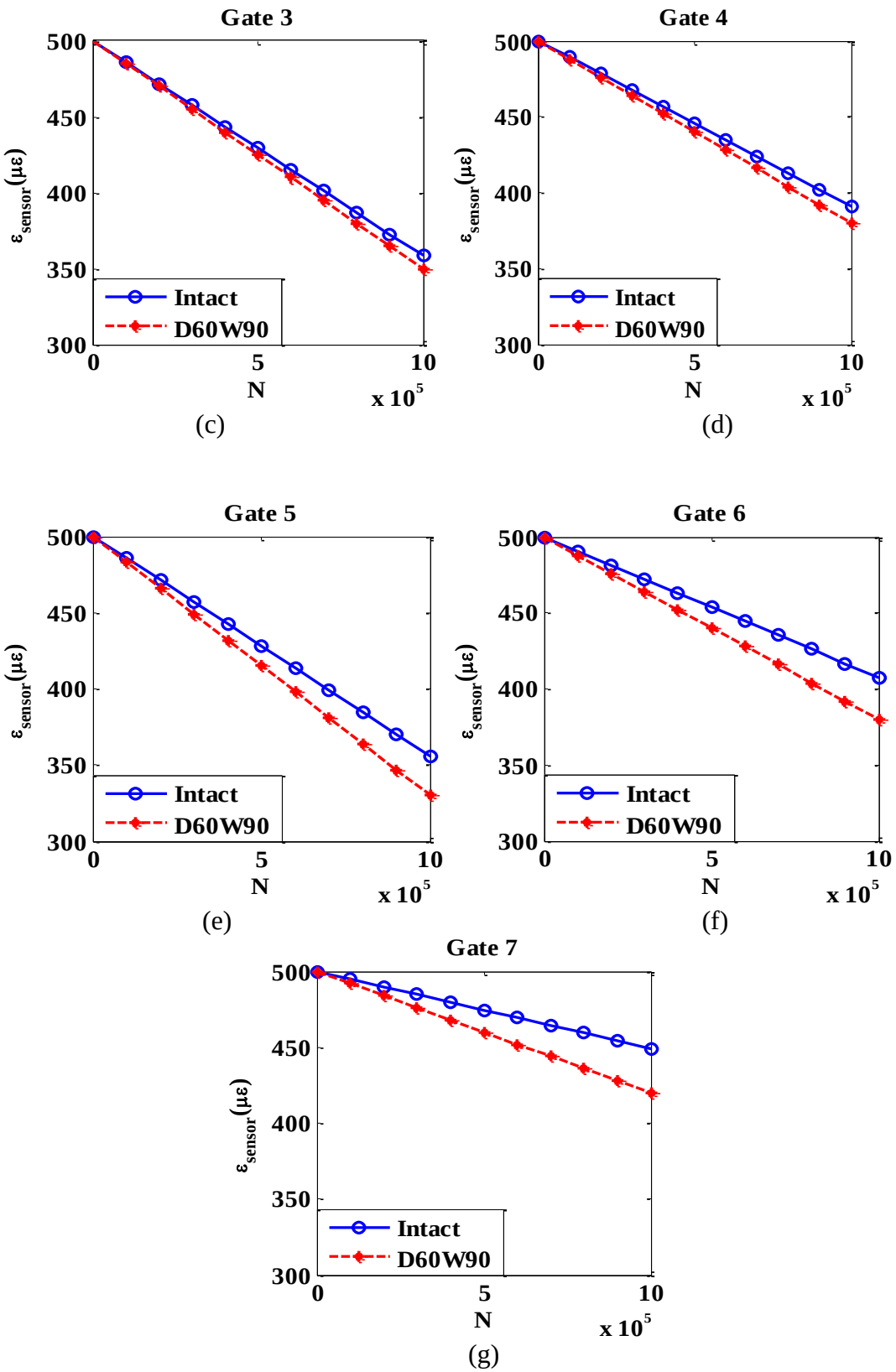

(c) (d) (e) (f) (g)

Fig. 17. Strain changes across sensor S1 gates vs number of cycles.

As can be seen in Fig. 17, the strain varies linearly as a function of the number of cycles. In addition, the slopes of the lines corresponding to the damaged pavement are higher (in absolute value) than the intact structure. This can be explained by the fact that the amplitude of strain continuously increases at location of sensor S1 with respect to the damage progression, and therefore, the cumulative time intersection increases as well.

3.2. Damage detection results

Although the output of the sensor changes with damage progression, there is a considerable loss of information. In fact, the sensor does not provide information about the strain distributions induced by service loads which makes the task of interpreting the sensor data a challenging task. Hasni et al. showed that for the case of a constant injection rate sensor, the cumulative time histogram can be characterized by a Gaussian cumulative density function (CDF) [20]. A CDF is fully defined by only two parameters: the mean and the standard deviation of the distribution. These parameters were shown to be good indicators of damage progression in structures [16-20]. On the other hand, when the gates have different injection rates, the output histogram cannot be fitted to a CDF. Accordingly, in this paper, a Gaussian mixture model (GMM) was proposed to fit the cumulative droppage of the strain at the sensing nodes. The GMMs are very powerful tools to adequately describe many types of data. In fact, certain models exhibit multimodalities that are poorly described by a single Gaussian distribution. In the case of different injection rates, the output histogram is expected to have different rate of strain variation between the gates resulting in multiple maxima. Therefore, a multi-modal Gaussian mixture (GM) model can be a good fit to the data. The probability density function (PDF) of a GM distribution is given by the following expression:

$$p(x) = \sum_{k=1}^{M} \frac{c_k}{\sqrt{2\,\pi\,{\sigma_k}^2}} \exp\left[-\frac{1}{2}\left(\frac{x-\mu_k}{\sigma_k}\right)^2\right] \quad (27)$$

where μ_k, σ_k $(k = 1..M)$ are mixture component parameters and c_k are the mixture weights. The mixture weights of the PDF should satisfy the following condition:

$$\sum_{k=1}^{M} c_k = 1 \quad (28)$$

In this paper, the strain droppage histogram was fitted by a bimodal GMM as follows:

$$\Delta\varepsilon(g) = \left(\sum_{i=1}^{7} \Delta\varepsilon_i\right) \sum_{k=1}^{2} \frac{\alpha_k}{\sqrt{2\,\pi\,{\sigma_k}^2}} \exp\left[-\frac{1}{2}\left(\frac{g-\mu_k}{\sigma_k}\right)^2\right] \quad (29)$$

where g is the gate number, (μ_k, σ_k) are the mixture components parameters, α_k is a parameter and $\Delta\varepsilon_i$ is the cumulative droppage in strain at gate number i. Eq. (29) has 6 parameters to estimate: μ_k, σ_k, α_k, k=1,2. These parameters can be obtained based on the 7 values of each gate of the sensor. Fig. 18 displays the obtained GMM fit to the data of sensor S1.

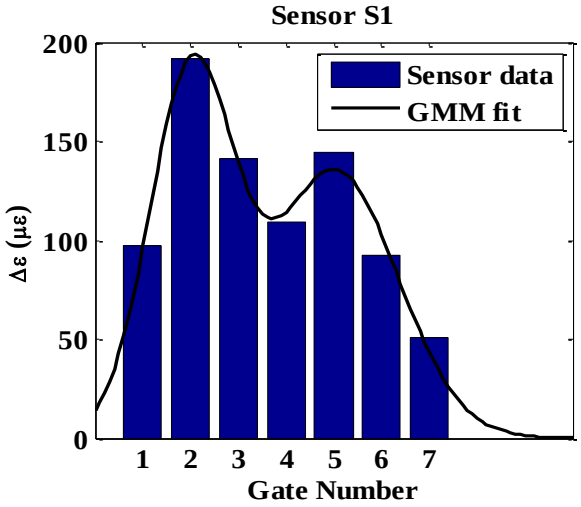

Fig. 18. GMM fit to sensor S1 data**.**

One million traffic cycles were applied to the pavement in order to get a significant droppage in the sensor output data. It is important to mention that the injection rates can be modified using an

additional resistance in parallel with the internal resistance of the sensor. Therefore, for a fatigue analysis, the impedance of the sensor should be increased in order to lower the gates injection rates. As seen in Fig. 18, the output histogram presents 2 peaks corresponding to the first two maximum strain drops. It is important to mention that the maximum values do not only depend on the injection rates, but they are also related to the threshold levels, the number of cycles and the strain rate variations. Fig. 19 displays the results of the GMM fit for different sensors. The GMM curves were plotted for the intact configuration and for D60W90 damage state. Based on the results, the GM distribution deviates from one damage states to another. According to section 2.7, the amplitude of the strain changes with damage growth. As a result, the cumulative time intersection changes as well and affects the variation of the strain at the sensor level.

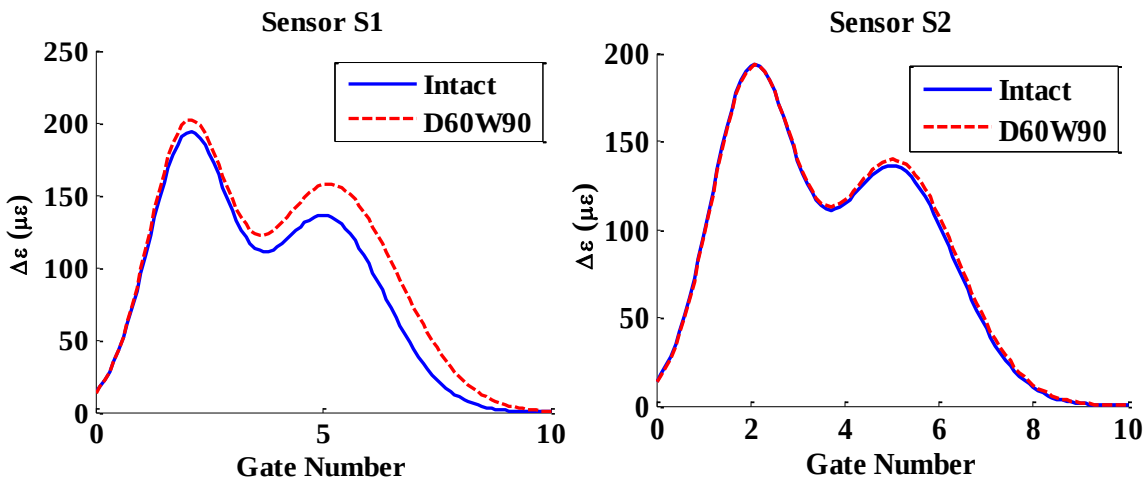

(a) (b)

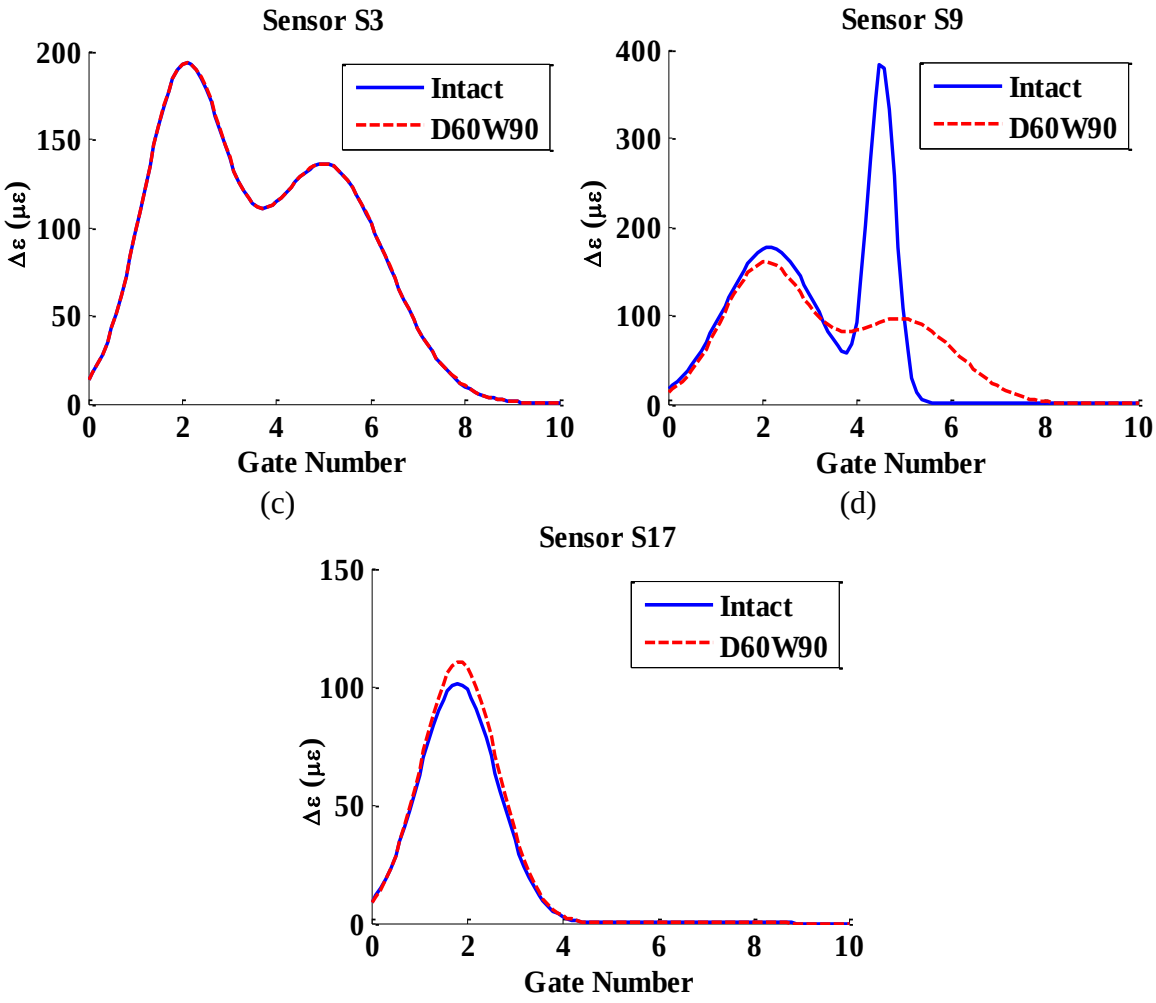

Fig. 19. GMM distributions for different sensors.

For sensor S1, the mean (μ_1) of the first components of the GM shifts to the left (decreases) and the second mean μ_2 shifts to the right (increases). In addition, the standard deviations σ_1 and σ_2 increase with damage progression as the distribution expands. Furthermore, when the sensor is located far from the damage zone, the variation of the GMM parameters becomes less significant as indicated by sensors S2 and S3. An interesting observation from the output of sensor S9 located at 60 mm offset from the x-axis is that σ_2 shows a significant variation between the intact and the damaged configurations. At the location of sensor S9, the maximum strain obtained by

the FE model was below 180 $\mu\varepsilon$ for the intact configuration. Therefore, gates 6 and 7 were still inactive and they did not record any data. When the damage reaches the D60W90 damage state, the maximum strain increased to 210.94$\mu\varepsilon$ which is above the maximum threshold level of all the gates. Thus, all the gates become active. When the output of sensor S9 is fitted by the GMM, the intact configuration presents a very small σ_2 and a mean μ_2 below 6 in order to satisfy the zero strain droppage condition described before. Thereafter, when all the gates become active at the last damage state (D60W90), the standard deviation of the second mixture component increases to 1.34 which is more than 16 times higher than σ_2 of the intact configuration. This considerably affects the width of the distribution.

For sensor S17, the amplitude of the strains was below 140 $\mu\varepsilon$ for both of the intact and the damaged configurations. Therefore, only the first 3 gates were active. On the other hand, all the sensors located at 180 mm offset from the x-axis, the strain amplitude is lower than the minimum threshold of the sensor. Thus, all the gates of these sensors remained inactive.

Based on the results, the bimodal GM parameters change due to the damage progression in the structure. Thus, the damage could be defined as function of these parameters as follows:

$$Damage = function\ (\mu_1, \sigma_1, \mu_2, \sigma_2) \tag{30}$$

However, the changes of the GM parameters are not always consistent. For example, for sensor S1, the first components (μ_1, σ_1) decrease and the second components (μ_2, σ_2) increase when damage progresses from the intact to D60W90 mode. For sensor S17, μ_1 and μ_2 increase and σ_1 and σ_2 decrease. Thus, it can be concluded that μ_1, σ_1, μ_2 and σ_2 are good damage indicators but cannot be individually used for classifying the damage state. To deal with this issue, a pattern recognition approach was developed to precisely detect and classify the damage phase.

4. Damage classification

4.1. Probabilistic neural network

Computational intelligence (CI) includes a set of nature-inspired approaches that can determine the model structure by automatically learning from data [15]. CI provides alternative solutions to overcome the limitations of the traditional mathematical modeling. These limitations might be associated with the uncertainties during the process, the complexity or the stochastic nature of the process. The CI techniques such as artificial neural network (ANNs), support vector machines (SVM), fuzzy inference system (FIS), etc have been widely used for behavioral characterization and health monitoring of pavements and infrastructure systems [45-49]. Major drawbacks of the widely-used ANNs are its 'black box' nature, the proneness to overfitting and the time-consuming iterative procedure required during training of the network to obtain the optimal learning parameters [50]. To overcome such limitations, PNN has been proposed by Specht [51]. One advantage of PNNs is that it does not have a separate training phase which makes the execution faster than the conventional neural networks.

PNN is a supervised neural network that is closely related to the standard Bayes classification rule and Parzen non-parametric PDF estimation technique. It is commonly used for pattern classification and recognition problems [50, 52, 53]. The Bayes formula can be expressed as follows:

$$P(\omega_j \mid x) = \frac{p(x \mid \omega_j) P(\omega_j)}{p(x)} \tag{31}$$

where $P(\omega_j|x)$ is the posterior probability, $P(\omega_j)$ is the prior probability and $P(x|\omega_j)$ is the likelihood of ω_j with respect to x. The Bayes decision rule is based on the maximization of the posterior probability. As the evidence p(x) is independent of the class label, then the decision rule can be determined by estimating the likelihood probability for each class and the priors.

The prior probability $P(\omega_j)$ highly depends on the specific task and should be decided by the physical knowledge of the problem. Thus, the only remaining unknown in the Bayes formula is the likelihood. This class conditional probability could be estimated using the non-parametric density estimation scheme using the Parzen window approach. More details about PNN can be found in [54, 55]. Assuming we have N training samples, $\{\mathbf{x_1},\ldots,\mathbf{x_N}\}$,divided into c classes, each of them has d dimension, and the h is the length of side of hypercube in the Parzen window approach. The estimation of density at a point **x** in the d dimensional space is:

$$p(x) = \frac{1}{N} \sum_{n=1}^{N} \frac{1}{h^d} k\left(\frac{x - x_n}{h}\right) \tag{32}$$

In Eq. (32), $k((\mathbf{x} - \mathbf{x}_n)/h)$ is the kernel function that is used to count the number of patterns located inside the hypercube of volume V = h^d. Similarly, the value of a probability density function of class ω_j is given by:

$$P_j(x) = \frac{1}{N_j} \sum_{n=1}^{N_j} \frac{1}{h^d}\ k\left(\frac{x - x_n^j}{h}\right) \tag{33}$$

When a Gaussian as kernel function is used, the final estimation becomes:

$$P_j(x) = \frac{1}{N_j} \sum_{n=1}^{N_j} \frac{1}{\sigma^d} \frac{1}{(2\pi)^{\frac{d}{2}}} \exp\left(-\frac{1}{2} \frac{\left\|x - x_n^j\right\|^2}{\sigma^2}\right) \tag{34}$$

The precedent expression can be written as follows:

$$P_j(x) = \frac{1}{N_j (2\pi)^{\frac{d}{2}} \sigma^d} \sum_{n=1}^{N_j} \exp\left(-\frac{\left\|x - x_n^j\right\|^2}{2\,\sigma^2}\right) \tag{35}$$

where N_j is the number of training patterns of class ω_j, σ is called the smoothing parameter that describes the spread of the Gaussian window function and $\boldsymbol{x_n^j}$ is the n^{th} pattern belonging to class ω_j. The feature vectors $\boldsymbol{x_n^j}$ represent the center of the Gaussian window. The smoothing parameter σ needs to be determined experimentally.

As mentioned before, the PNN structure is a direct implementation of the PDF estimator (Eq. (35)) and the Bayesian decision rule. A typical PNN with 4-layers architecture is shown in Fig. 20. The network is constructed by the following layers: input layer, pattern layer, summation layer and output layer. The input layer consists of d input units, which corresponds to the d features. Each input unit is connected to each of the N pattern units [15]. The number of nodes in the pattern layer is equal to the total number of training vectors. Each pattern unit k computes the inner product of its weight vector and the normalized pattern vector **x** as follows:

$$net_k = \boldsymbol{w_k^t}\, \boldsymbol{x} \tag{36}$$

Thereafter, each pattern unit emits a nonlinear transfer function:

$$\exp\left(\frac{\boldsymbol{net_k}-1}{\sigma^2}\right) = \exp\left(\frac{\boldsymbol{w_k^t}\, \boldsymbol{x}-1}{\sigma^2}\right) \tag{37}$$

On the other hand, the desired Gaussian window function is:

$$k\left(\frac{\boldsymbol{x}-\boldsymbol{w_k}}{h}\right) \propto \exp\left(-\frac{(\boldsymbol{x}-\boldsymbol{w_k})^t(\boldsymbol{x}-\boldsymbol{w_k})}{2\sigma^2}\right) = exp\left(\frac{2\boldsymbol{x^t w_k}-\boldsymbol{x^t x}-\boldsymbol{w_k^t w_k}}{2\sigma^2}\right) \tag{38}$$

By taking into account the normalization of **x** and $\boldsymbol{w_k}$, Eq. (38) can be expressed as follows:

$$k\left(\frac{\boldsymbol{x}-\boldsymbol{w_k}}{h}\right) \propto exp\left(\frac{\boldsymbol{x^t w_k}-1}{\sigma^2}\right) = nonlinear\ transfer\ function \tag{39}$$

The precedent equation explains the choice of the nonlinear transfer function employed by the pattern units.

Each neuron in the summation layer will sum these functions corresponding to a single population. As a result, the output of the summation layer has the same form as the Parzen window estimate of the distribution. The output of the summation layer is:

$$C_j(x) = \sum_{k=1}^{N_j} \exp\left(\frac{\boldsymbol{x^t w_{jk}}-1}{\sigma^2}\right) \tag{40}$$

Thereafter, if the prior probabilities are the same and the cost functions of making an incorrect decision are the same for all classes, the decision layer classifies according the Bayes decision rule as follows:

$$C(x) = \underset{j=1..c}{argmax}\, P_j(x) \tag{41}$$

The training of PNN is fast, and it guarantees the convergence to an optimal classifier as the size of training samples increases. Also, PNN does not have local minima problems. However, one major challenge is to find the optimal smoothing parameter σ. A very small σ can produce many empty hypercube and may result in problems of overfitting. On the other hand, if the window width is too large, the PNN classifier may under-fit the data as it cannot present some important local variations. Therefore, the accuracy of the PNN classifier highly dependents on the choice of the smoothing parameter [15].

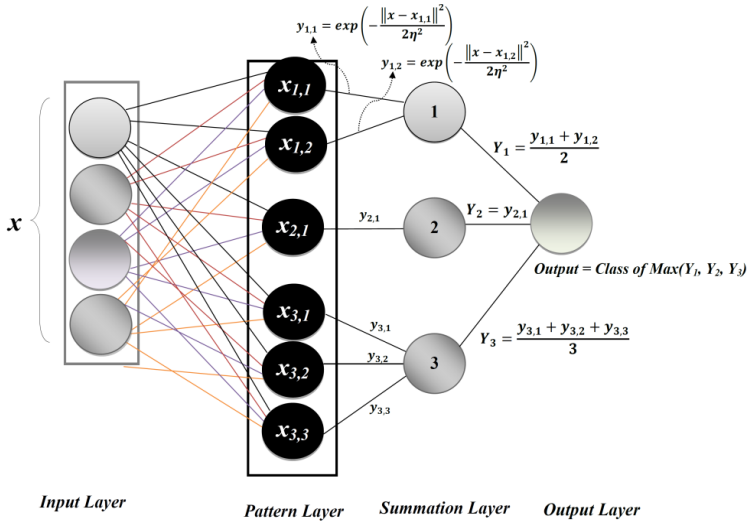

Fig. 20. A typical architecture of PNN.

As mentioned before, 32 sensors were defined on the surface of the pavement. However, only 15 sensors were considered in this analysis for the following two reasons:

- The maximum strain at the 180 mm offset set of sensors is below the minimum threshold of the sensor.

- The difference on the peak strain values for last 3 sensors of each set between any two damage states is very low.

Therefore, only sensors S1, S2, S3, S4, S5, S9, S10, S11, S12, S13, S17, S18, S19, S20, and S21 were used in the analysis. In addition, the damage states were divided into 4 classes as follows:

ω_1: Intact structure

ω_2: D20W30, D20W50, D20W70, D20W90

ω_3: D40W30, D40W50, D40W70, D40W90

ω_4: D60W30, D60W50, D60W70, D60W90

Each sensor represents a pattern for the classifier, therefore the total number of data points is: 15 × 13 = 195. The performance of the developed models was measured using the Detection Rate (DR):

$$DR = \frac{Number\ of\ Patterns\ Correctly\ Classified}{Total\ Number\ of\ Patterns} \tag{42}$$

4.2. Performance of the initial features

The initial feature vectors were defined based on the GMM parameters ($\mu_1, \sigma_1, \mu_2, \sigma_2$). These parameters were used to characterize the initial input vector $\underline{x}$ as follows:

$$\underline{x} = [x_1 x_2 x_3 x_4]^t \tag{43}$$

where

$$\begin{cases} x_1 = \mu_1 \\ x_2 = \sigma_1^2 \\ x_3 = \mu_2 \\ x_4 = \sigma_2^2 \end{cases} \tag{44}$$

As indicated by Eq. (43), the initial problem has 4 dimensions. Thus, 195 4-dimenstional patterns were used for the classification. The total number of data was divided into 3 sets:

- 70 % training = 137 input vector
- 15 % validation = 29 input vector
- 15 % testing = 29 input vector

As one would expect, these 4 initial features provided very low accuracy on the validation and testing data. The maximum detection rates for the validation and testing data were 27.58% and 13.79%, respectively. Fig. 21 displays the results of the classification in the validation set as a function of the PNN smoothing parameter (σ). Multiple iterations were performed by varying the smoothing parameter in order to find the optimal value that gives the best accuracy on the validation set. The best configuration was then applied to the unseen testing data. As seen in Fig. 21, the best detection rate was obtained when the optimal smoothing parameter is between 1 and 10. Hence, the optimum value of σ is equal to 1.

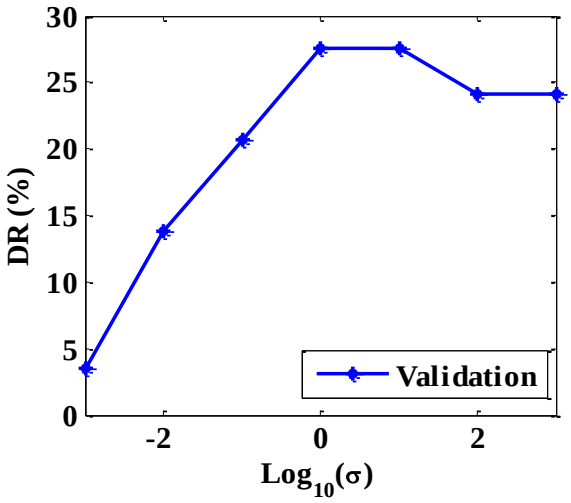

Fig. 21. Accuracy versus smoothing parameter for the validation set.

Thereafter, a Principal Component Analysis (PCA) was performed on the initial set of patterns in order to visualize the data along its first two principal components. This method can reduce a high-dimensional space to a lower-dimensional space that optimally describes the highest variance of the data. Fig. 22 displays the original input data ($\underline{x}$) projected on the two first principal components. The obtained eigenvalues of the covariance matrix are: $\lambda_1 = 152.49$, $\lambda_2 = 1.61$, $\lambda_3 = 0.02$, $\lambda_4 = 1.57 \times 10^{-4}$. Hence, the first two components represent 99.99 % of the data. The detection accuracy using the reduced feature vector: $\underline{x'} = [x_1\ x_2]^t$ was increased from 13.79 % to 34.48 % for the testing data. Furthermore, as seen in Fig. 22, the defined 4 damage classes overlap intensively which results in a low detection accuracy.

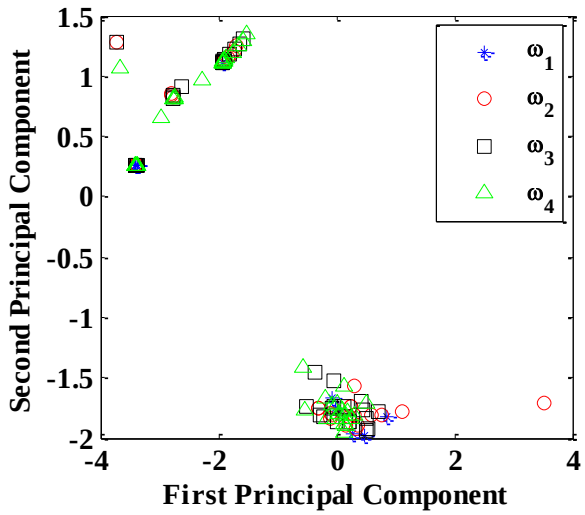

Fig. 22. Projection of the data onto the first two principal components.

4.3. Data fusion model

4.3.1. Feature transformation

According to the preliminary results, the initial input feature vector $\underline{x}$ did not contain enough information to separate classes. Hence, a new strategy was defined to improve the damage

detection performance. On this basis, it was decided to fuse both the information provided by one sensor and all the information supplied by the other sensors. This approach is also known as 'group effect' of sensors [17, 18]. In this case, even if one sensor does not sense the damage, the group effect (sensors network) will help detect the damage class. Fig. 23 summarizes the proposed method for the data fusion model.

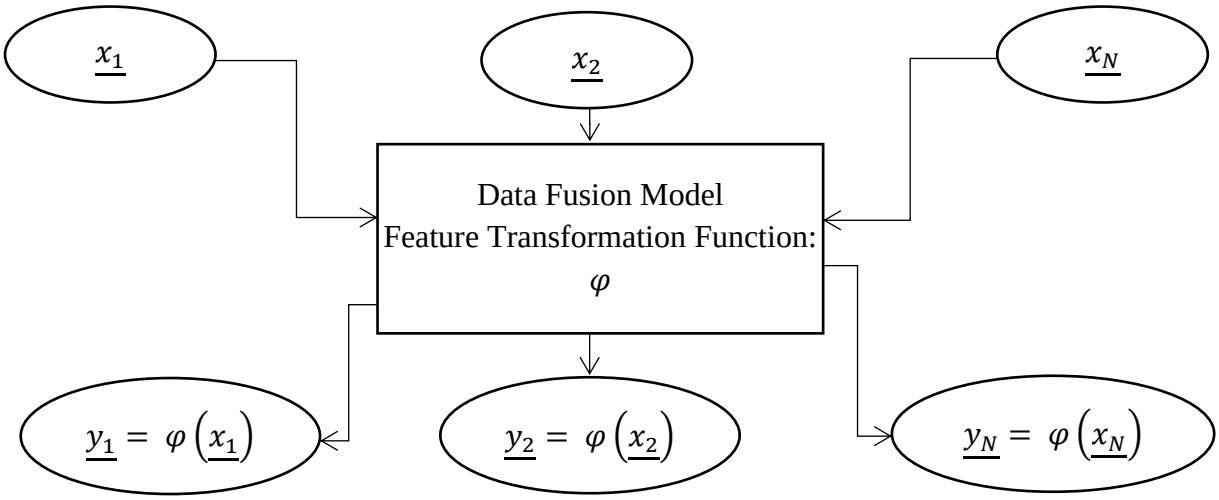

Fig. 23. Data fusion model.

The proposed feature transformation function φ could be written as follows:

$$\varphi: \mathbb{R}^4 \xrightarrow{feature\ transformation} \mathbb{R}^{10}$$

$$\underline{x} = [x_1\ x_2\ x_3\ x_4] \xrightarrow{\varphi} \underline{y} = [y_1\ y_2\ y_3\ y_4\ y_5\ y_6\ y_7\ y_8\ y_9\ y_{10}] \tag{45}$$

The new set of features were introduced to the formulation of the problem as follows:

$$\underline{y} = \begin{cases} y_1 = \frac{x_1 - x_{1_{\text{ave}}}}{x_{1_{\text{STD}}}} \\ y_2 = \frac{x_2 - x_{2_{\text{ave}}}}{x_{2_{\text{STD}}}} \\ y_3 = \frac{x_3 - x_{3_{\text{ave}}}}{x_{3_{\text{STD}}}} \\ y_4 = \frac{x_4 - x_{4_{\text{ave}}}}{x_{4_{\text{STD}}}} \\ y_5 = \frac{x_1 - x_{1_{\text{STD}}}}{x_{1_{\text{ave}}}} \\ y_6 = \frac{x_2 - x_{2_{\text{STD}}}}{x_{2_{\text{ave}}}} \\ y_7 = \frac{x_3 - x_{3_{\text{STD}}}}{x_{3_{\text{ave}}}} \\ y_8 = \frac{x_4 - x_{4_{\text{STD}}}}{x_{4_{\text{ave}}}} \\ y_9 = \frac{(x_1 + x_3) - (x_{2_{\text{ave}}} + x_{4_{\text{ave}}})}{x_{1_{\text{ave}}} + x_{3_{\text{ave}}}} \\ y_{10} = \frac{(x_2 + x_4) - (x_{1_{\text{ave}}} + x_{3_{\text{ave}}})}{x_{2_{\text{ave}}} + x_{4_{\text{ave}}}} \end{cases} \quad (46)$$

where

- x_i: The i[th] feature of the initial feature vector,
- $x_{i_{\text{ave}}}$: The average of x_i for all patterns corresponding to a specific damage state,
- $x_{i_{\text{STD}}}$**:** The standard deviation of x_i for all patterns corresponding to a specific damage state.

The new defined features y_i (i=1..10) were derived from the conventional z-score function. In fact, features y_1 to y_4 are the z-score functions and features y_5 to y_{10} are functions that are inspired from the form of the conventional z-score function. All the y_i (i=1..10) were based on the average and the standard deviation of all patterns of a specific damage state.

4.3.2. Feature selection

The new features were expected to increase the 'distance' between classes especially between two consecutive damage states. The word distance here refers to Euclidian distance between two features in the d-dimensional space belonging to two different classes. Furthermore, by

increasing the dimensionality of the problem from 4 to 10, the accuracy is more likely to increase. However, increasing the number of features may also lead on the curse of dimensionality. Therefore, different feature selection methods were used to tackle this problem. In this paper, sequential forward selection (SFS), sequential backward selection (SBS) and exhaustive search (brute-force search) algorithms were used to select the best set of features [56-59].

SFS: SFS sequentially adds the best feature y^+ that maximizes the objective function $J(Z_k + y^+)$. The SFS algorithm works as follows [59]:

1. Start with the empty set $Z_0 = \{\emptyset\}$

2. Select the next best feature: $y^+ = \underset{y \notin Z_k}{argmax}(J(Z_k + y))$

3. Update $Z_{k+1} = Z_k + y^+$; $k = k + 1$

Go to 2

Table 5 displays the sets selected by the SFS algorithm and their performances at each step. The best accuracy on the training, validation and testing data was obtained using the feature vectors Z_8 or Z_9 selected as follows:

$$Z_8 = \{y_9, y_1, y_2, y_3, y_4, y_5, y_6, y_7\} \quad (47)$$

$$Z_9 = \{y_9, y_1, y_2, y_3, y_4, y_5, y_6, y_7, y_8\} \quad (48)$$

The detection rate accuracy using feature vectors Z_8 or Z_9 was 100%, 96.55% and 93.10% for the training, validation and testing data, respectively. The optimal smoothing parameter was calculated at each iteration of the algorithm.

Table 5. Features selected by SFS and their corresponding detection rates.

Set Number	Features	Training Accuracy (%)	Validation Accuracy (%)	Testing Accuracy (%)

1	$\{y_9\}$	94.89	89.65	89.65
2	$\{y_9, y_1\}$	100	89.65	93.10
3	$\{y_9, y_1, y_2\}$	100	79.31	93.10
4	$\{y_9, y_1, y_2, y_3\}$	100	79.31	93.10
5	$\{y_9, y_1, y_2, y_3, y_4\}$	100	79.31	93.10
6	$\{y_9, y_1, y_2, y_3, y_4, y_4\}$	100	82.75	93.10
7	$\{y_9, y_1, y_2, y_3, y_4, y_4, y_5\}$	100	82.75	93.10
8	$\{y_9, y_1, y_2, y_3, y_4, y_5, y_6, y_7\}$	100	96.55	93.10
9	$\{y_9, y_1, y_2, y_3, y_4, y_5, y_6, y_7, y_8\}$	100	96.55	93.10
10	$\{y_9, y_1, y_2, y_3, y_4, y_5, y_6, y_7, y_8, y_{10}\}$	100	96.55	89.65

SBS: This method sequentially removes the worst feature y^-that least reduces the objective function $J(Z_k - y^-)$. The SBS algorithm works as follows [59]:

1. Start with the full set $Z_0 = \underline{y}$,

2. Remove the worst feature: $y^- = \underset{y \in Z_k}{\operatorname{argmax}}(J(Z_k - y))$

3. Update $Z_{k+1} = Z_k - y^-$; $k = k + 1$.

Go to 2

Table 6 displays the sets selected by the SBS algorithm at each step. The best accuracy on the training, validation and testing data was obtained using feature vectors Z_1, Z_2 or Z_3, where:

$$Z_1 = \{y_2, y_3, y_4, y_5, y_6, y_7, y_8, y_9, y_{10}\} \quad (49)$$

$$Z_2 = \{y_3, y_4, y_5, y_6, y_7, y_8, y_9, y_{10}\} \quad (50)$$

$$Z_3 = \{y_3, y_4, y_5, y_6, y_7, y_8, y_9\} \quad (51)$$

The best detection accuracy was 100%, 96.55%, 93.10% for the training, validation and testing data, respectively. Multiple iterations were performed at each step to find the optimal smoothing parameter. The optimal set extracted by the SBS algorithm is Z_3 which has 7 dimensions.

Table 6. Features selected by SBS and their corresponding detection rates.

Set Number	Features	Training Accuracy (%)	Validation Accuracy (%)	Testing Accuracy (%)
1	$\{y_1, y_2, y_3, y_4, y_5, y_6, y_7, y_8, y_9, y_{10}\}$	100	96.55	89.65
2	$\{y_2, y_3, y_4, y_5, y_6, y_7, y_8, y_9, y_{10}\}$	100	96.55	93.10
3	$\{y_3, y_4, y_5, y_6, y_7, y_8, y_9, y_{10}\}$	100	96.55	93.10
4	$\{y_3, y_4, y_5, y_6, y_7, y_8, y_9\}$	100	96.55	93.10
5	$\{y_4, y_5, y_6, y_7, y_8, y_9\}$	100	96.55	89.65
6	$\{y_5, y_6, y_7, y_8, y_9\}$	100	96.55	86.20
7	$\{y_6, y_7, y_8, y_9\}$	100	96.55	86.20
8	$\{y_7, y_8, y_9\}$	100	96.55	86.20
9	$\{y_8, y_9\}$	98.54	93.10	86.20
10	$\{y_9\}$	94.89	89.65	89.65

Exhaustive search: The main limitation of SFS pertains to the fact that it is unable to remove feature that become obsolete after the addition of other features. Similarly, SBS cannot reevaluate the usefulness of a removed feature on the selected set [61]. Both algorithms are suboptimal. Therefore, an exhaustive search algorithm was performed. It was decided to select the best 3 features that give the best classification accuracy. As the problem has 10 dimensions, the algorithm performed $C_{10}^{3} = 120$ iterations in order to find the best set of 3 features. One the best obtained sets that gives the best accuracy is:

$$S_{optimal} = \{y_4, y_7, y_9\} \tag{52}$$

The detection rate for the training, validation and testing data was equal to 100%, 96.55% and 93.10%, respectively. Fig. 24 displays the confusion matrixes. A confusion matrix is a table that displays the performance of the classification. The rows represent the actual class and the columns represent the predicted class. As observed from the confusion matrixes, only 2 patterns were misclassified in the testing set and 1 pattern in the validation set. The obtained optimal smoothing parameter was 0.01 (Fig. 25).

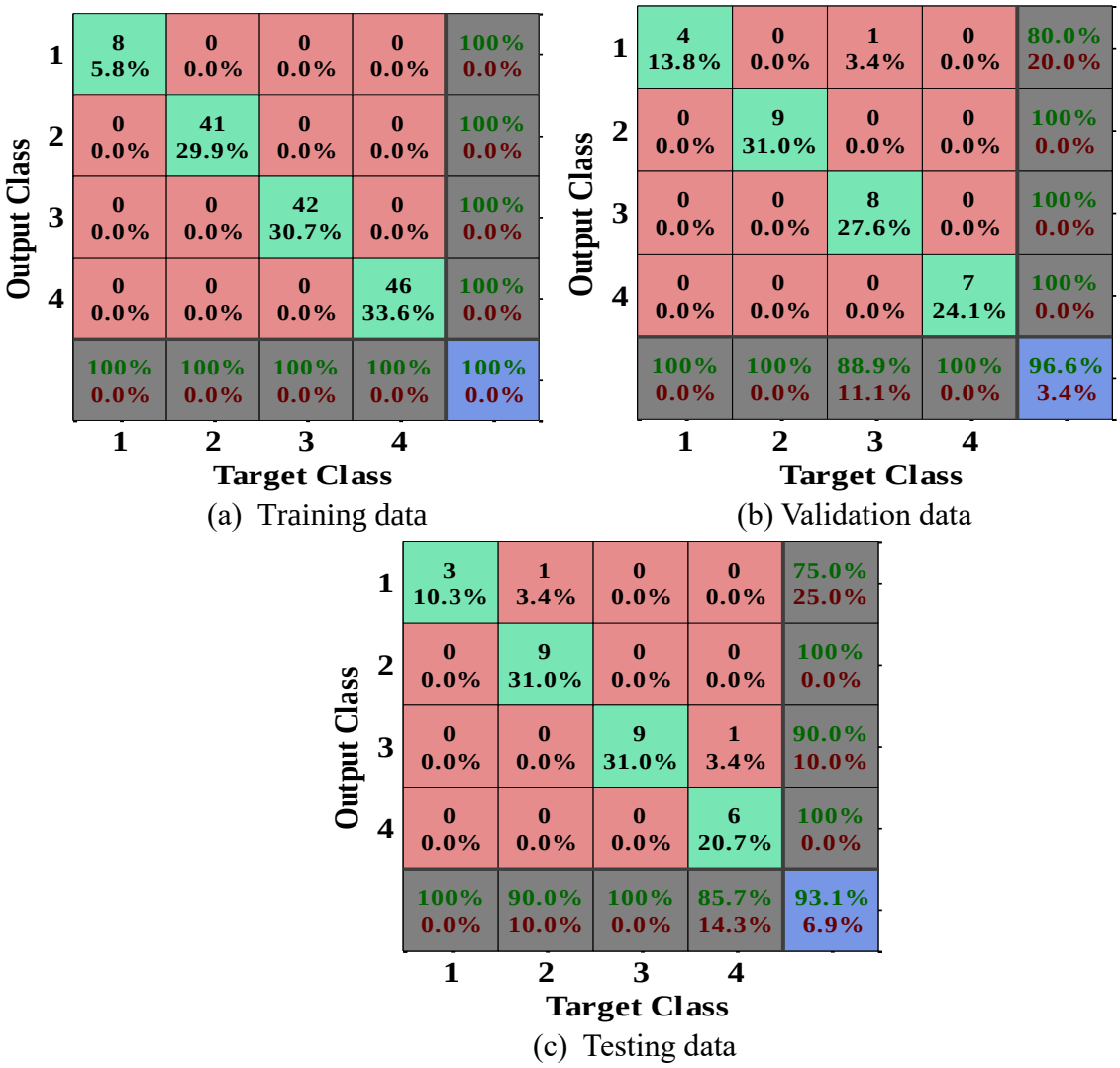

Fig. 24. Confusion matrixes using the best features selected by the exhaustive search method.

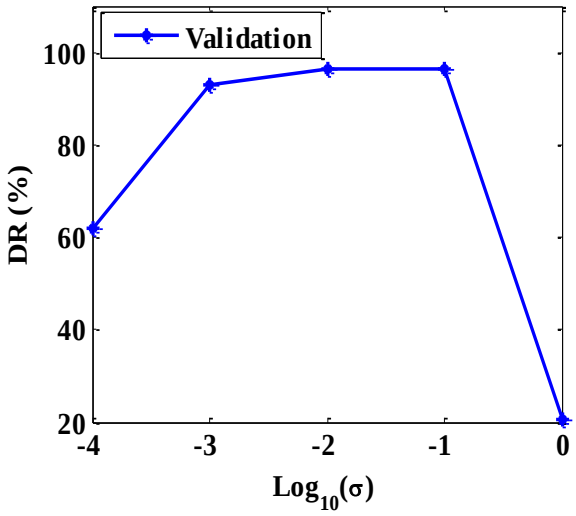

Fig. 25. Accuracy versus smoothing parameter for the validation set.

The new set of features based on the data fusion model has enhanced the performance of the detection rate from 13.79 % to 93.1 % on the testing set. This new set of predictors was inspired form the conventional z-score function and is based on the average and standard deviation of a group of patterns. Fig. 26 shows the distribution of the data using the optimal set of features. As seen in this figure, the classes are more separable compared to the initial input data.

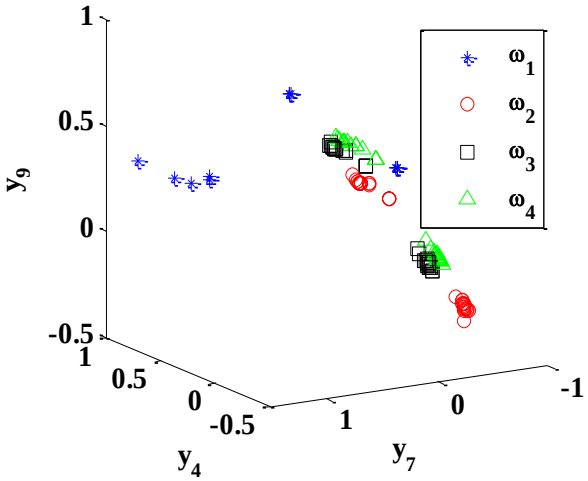

Fig. 26. Distribution of the new data using the optimal set of features.

4.4. Uncertainty analysis

In this paper, the sensor data was simulated using the strain history provided by the FE analysis of the pavement under different damage scenarios. However, different sources of uncertainties can contribute to an error between the FE modeling and the real structural behavior [60]. On this basis, an uncertainty analysis can enhance the reliability of the proposed damage detection approach. To this aim, the input data was polluted using a Gaussian noise with 5 different levels: 10%, 20%, 30%, 40% and 50%. The best set of predictors $S_{optimal}$ was used in the noise pollution verification phase. Thereafter, the PNN algorithm was run for all the noise levels. For each case, the optimal smoothing parameter was calculated. Table 7 presents the results of the uncertainty analysis. As seen in Table 7, the performance of the models remains satisfactory up to a 30% noise level. The detection rates for a noise level below or equal to 30% are above 82 % for the training, validation and testing sets.

Table 7. Damage detection performance for various noise levels using the optimal set of features.

Noise Level	Optimal smoothing parameter	Damage Detection Performance (%)		
		Training	Validation	Testing
10%	1E-2	100	96.55	89.65
20%	1E-2	100	82.75	86.20
30%	1E-2	100	86.20	86.20
40%	1E-1	87.59	72.41	75.86
50%	1E-2	100	72.41	75.86

5. Summary and conclusions

This paper presents a new approach for pavement health monitoring based on a self-powered surface sensing technology. The self-powered sensor operates by harvesting the strain energy

from the host structure and records the cumulative droppage of the strain. Each sensor has seven memory gates for data storage. Each gate has an activation threshold level from which the sensor start recording the cumulative droppage of the strain. Moreover, each gate has a specific injection rate which controls the speed of the variation of the strain (strain droppage) at the sensor gates. These injection rates can be modified by adding load resistance on the sensor interface board depending on the nature of the application. The difference between the previously used sensors (constant injection rate sensors) is the variability of the injection rates between the gates which makes the interpretation of the data more complicated. Therefore, a new strategy was proposed for data fitting and interpretation using the non-constant injection rate class of sensors. The main focus of this study is the detection of bottom up cracking in the AC pavements using sensors located near the surface of the layer. In particular, such surface sensing technology is important for the monitoring of existing pavements. In order to verify the performance of the proposed method, 3D FE models of a pavement structure were created using ABAQUS. Subsequently, the principal strain time-histories were extracted for different sensing nodes from the surface of the AC layer. The pavement was subjected to a dynamic moving load at highway speed. The models incorporated the tire-pavement contact stress, a viscoelastic behavior for HMA, an elastic behavior with damping for base and subgrade and a continuous moving load. The moving load was created via a DLOAD subroutine using FORTRAN. Thereafter, different damage scenarios were introduced to the bottom of the AC layer. The damage states were defined based on the EWM by reducing the material properties of the AC layer and varying the dimensions of the damaged volume. The FE results show that the strain amplitude changes as a function of the damage state. In addition, the location of the sensor with respect to the damage controls the variation of the strain amplitudes. The sensor output was

calculated based on the FE strain history. Based on the results, it was found that the damage could be detected through the strain droppage of the sensor gates. However, only the sensors at a specific location with respect to the damage location were sensitive to the damage progression. To tackle this problem, different stages were considered for the performance verification of the proposed approach. At the first stage, the complicated histogram of sensor data was fitted by a bi-modal GM model in order to define initial damage indicators. The results show that the bi-modal GM parameters are good damage indicators only at specific locations. Thus, in the second step, a data fusion model was proposed by defining new descriptive features from the GMM parameters. These new predictors contained the information supplied by the all the sensors at each specific sensing node. Thereafter, different feature extraction methods (SFS, SBS, exhaustive search) were used to check the curse of dimensionality and to select the optimal set of features that gives the best accuracy. A PNN classification scheme was used to classify the predefined damage stages. The results showed that using the optimal set of predictors could provide satisfactory detection rate accuracy (100% on the training data, 96.6% on the validation data and 93.1% on the testing data). Finally, an uncertainty analysis was performed to simulate the performance of the sensor under real operating conditions and to take into account the errors of the numerical modeling. A Gaussian noise with different levels was applied to the data. The detection performance remained satisfactory up to 30% noise level. While the proposed approach has provided sound results, there are still some challenges to be addressed in future studies:

- The conducted analyses were based on discrete damage states, while cracking is a continuous phenomenon in reality. Hence, developing FE models with continuous damage propagation can result in a more realistic detection approach.
- The effect of high or low temperatures on the sensor output needs more research.

- Reliability of the sensor under different environmental and operating conditions should be evaluated more in-depth.
- Verification of the long-term performance of the proposed approach for a real-life structure is also an interesting topic for future study.
-

Acknowledgment

The presented work is supported by a research grant from the Federal Highway Administration (FHWA) (DTFH61-13-C-00015).

References

[1] D. Cebon, Road damaging effects of dynamic axle loads, In: Proceedings of the international symposium on heavy vehicle weights and dimensions, Kelowna, BC, Canada. (1986) 37-53.

[2] P.J. Yoo, I.L. Al-Qadi, Effect of Transient Dynamic Loading on Flexible Pavements, Transportation Research Record, 1990, Transp. Res. Board National Acade. Washington, DC. (2007) 129-140.

[3] T.D. Gillespie, S.M. Karimihas, D. Cebon, M.W. Sayers, M.A. Nasim, W. Hansen, N. Ehsan, NCHRP Report 353: Effect of Heavy Vehicle Characteristics on Pavement Response and Performance, TRB, National Res. Council, Washington, D.C., 1993.

[4] J.P. Lourens, Nonlinear Dynamic Analysis and Design of Road Pavements, RR 90/030, Department of Transport, Pretoria, South Africa, 1992.

[5] I.L. Al-Qadi, A. Loulizi, M. Elseifi, S. Lahouar, The Virginia smart road: the impact of pavement instrumentation on understanding pavement performance, J. Assoc. Asphalt Paving Tech. 73 (2004) 427–465.

[6] M.A. Elseifi, , I.L. Al-Qadi, , P.J. Yoo, Viscoelastic modeling and field validation of flexible pavements, J. Eng. Mech. 132(2) (2006) 172-178.

[7] S. Yang, H. Ceylan, K. Gopalakrishnan, S. Kim, Smart airport pavement instrumentation and health monitoring, Civ. Construct. Env. Eng. Conf. Present. Proc. (2014) 8.

[8] W. Xue, Integrated Transportation Monitoring System for Both Pavement and Traffic, PhD Thesis, Virginia Polytechnic Institute and State University, Blacksburg, VA, 2013.

[9] Z.J. Dong, S.L. Li, J.Y. Wen, H.C. Chen, Asphalt Pavement Structural Health Monitoring Utilizing FBG Sensors, Adv. Eng. Forum. 5 (2012) 339-344.

[10] N. Lajnef, K. Chatti, S. Chakrabartty, M. Rhimi, P. Sarkar, Smart Pavement Monitoring System, Report: FHWA-HRT-12-072, Fed. Hwy. Administ. (FHWA), Washington, D.C., 2013.

[11] R. Bennett, B. Hayes-Gill, J.A. Crowe, R. Armitage, D. Rodgers, A. Hendroff, Wireless Monitoring of Highways. Smart Syst. Bridges, Struct. Highways, Proc. SPIE, Newport Beach, CA, 3671 (1999) 173-182.

[12] N. Attoh-Okine, S. Mensah, MEMS Application in Pavement Condition Monitoring-Challenges, NIST Special Publication SP, (2003) 387-392.

[13] H. Ceylan, K. Gopalakrishnan, S. Kim, P.C. Taylor, M. Prokudin, A.F. Buss, Highway Infrastructure Health Monitoring Using Micro-Electromechanical Sensors and Systems (MEMS). J. Civ. Eng. Mgmt. 19 (sup1) (2013)188-201.

[14] A.H. Alavi, H. Hasni, N. Lajnef, K. Chatti, F. Faridazar, Continuous Health Monitoring of Pavement Systems Using Smart Sensing Technology, Constr. Build. Mater. 114 (2016) 719-736.

[15] A.H. Alavi, H. Hasni, N. Lajnef, K. Chatti, F. Faridazar. An intelligent structural damage detection approach based on self-powered wireless sensor data, Auto. Const. 62 (2016) 24-44.

[16] A.H. Alavi, H. Hasni, N. Lajnef, K. Chatti, F. Faridazar, Damage Detection Using Self-Powered Wireless Sensor Data: An Evolutionary Approach, Meas. 82 (2016) 254-283.

[17] A.H. Alavi, H. Hasni, N. Lajnef, K. Chatti, Damage growth detection in steel plates: Numerical and experimental studies, Eng. Struct. 128 (2016) 124-138.

[18] H. Hasni, A.H. Alavi, P. Jiao, N. Lajnef, Detection of fatigue cracking in steel bridge girders: A support vector machine approach, Arch. Civ. Mech. Eng. 17(3) (2017) 609-622.

[19] P. Jiao, W. Borchani, H. Hasni, A.H. Alavi, N. Lajnef, Post-buckling response of non-uniform cross-section bilaterally constrained beams, Mech. Res. Commun. 78 (2016) 42-50.

[20] C. Huang, N. Lajnef, S. Chakrabartty, Self-calibration and characterization of self-powered floating-gate usage monitors with single electron per second operational limit, IEEE Trans. Biomed. Circuits Syst. 57 (2010) 556-567.

[21] N. Lajnef, M. Rhimi, K. Chatti, L. Mhamdi, Toward an Integrated Smart Sensing System and Data Interpretation Techniques for Pavement Fatigue Monitoring, Comput.-Aided Civ. Infrastruct. Eng. 26 (2011) 513-523.

[22] K.R. Maser, Condition assessment of transportation infrastructure using ground-penetrating radar, J. Infrastruct. Syst. 2(2) (1996) 94-101.

[23] ABAQUS, ABAQUS/CAE User's Manual, Version 6.10, Dassault Systèmes, 2010.

[24] I.L. Al-Qadi, H. Wang, E. Tutumluer, Dynamic analysis of thin asphalt pavements utilizing cross-anisotropic stress-dependent properties for granular layer, Transp. Res. Rec. 2154 (2010) 156-163.

[25] H. Wang, Analysis of tire-pavement interaction and pavement responses using a decoupled modeling approach, PhD Dissertation in Civil Engineering, Univ. Illinois Urbana-Champaign, 2011.

[26] J.M. Duncan, C.L. Monismith, E.L. Wilson, Finite element analysis of pavements, Hwy. Res. Rec. 228 (1968) 18-33.

[27] A.K. Chopra, Dynamics of Structures, 2nd ed., Prentice Hall, Upper Saddle River, NJ, 2001.

[28] K.J. Bathe, Finite element procedures, Englewood Cliffs, NJ: Prentice Hall, 1996.

[29] R. Michalczyk, Implementation of Generalized Viscoelastic Material Model in Abaqus Code, Logistyka, 6 (2011).

[30] R.V. Siddharthan, J. Yao, P.E. Sebaaly, Pavement strain from moving dynamic 3D load distribution, J. Transp. Eng. 124(6) (1998) 557-566.

[31] J.T., Tielking, F.L. Roberts, Tire contact pressure and its effect on pavement strain, J. Transp. Eng. 113(1) (1987) 56-71.

[32] F. Wang, R.B. Machemehl, Mechanistic-emperical study of effects of truck tire pressure on pavement: measured tire-pavement contact stress data, Transportation Research Record 1947, TRB, National Research Council, Washingon D.C., (2006) 136-145.

[33] Z.Q. Yue, O.J. Svec, Effects of tire-pavement contact pressure distributions on the response of asphalt concrete pavemens, Canadian J. Civ. Eng. 22(5) (1995) 849-860.

[34] W. Alkasawneh, E. Pan, R. Green, The effect of loading configuration and footprint geometry on flexible pavement response based on linear elastic theory, Road Mater. Pav. Eng. 9(2) (2008) 159-179.

[35] S. Mun, M.N. Guddati, Y.R. Kim, Viscoelastic continuum damage finite element modeling of asphalt pavements for fatigue cracking evaluation, KSCE J. Civ. Eng. 10(2) (2006) 97-104.

[36] S. Weissman, Influence of tire-pavement contact stress distribution on development of distress mechanisms in pavements, Transp. Res. Rec. 1655, TRB, National Res. Council, Washington D.C. (1999) 161-167.

[37] J. Perret, A. Dumont, Strain and stress distributions in flexible pavements under moving loads, Road Mater. Pav. Des. 5(1) (2004) 203-225.

[38] I.L. Qadi, H. Wang, Pavement Damage Due to Different Tire and Loading Configurations on Secondary Roads, NEXTRANS Univ. Transp. Center, West Lafayette, IN, 2010.

[39] C. Huang, R.K. Abu Al-Rub, E.A. Masad, D.N. Little, Three-dimensional simulations of asphalt pavement permanent deformation using a nonlinear viscoelastic and viscoplastic model, J. Mater. Civ. Eng. 23(1) (2011) 56-68.

[40] A. Sarkar, Numerical comparison of flexible pavement dynamic response under different axles, Int. J. Pav. Eng. 17(5) (2016) 377-387.

[41] G. Shafabakhsh, H. Naderpour, M. Motamedi, Dynamic analysis and determination of maximum tensile strain of bottom asphalt concrete for different vehicle velocities, Eng. J. 19(4) (2015) 107-116.

[42] E.V. Dave, W.G. Buttlar, Thermal reflective cracking of asphalt concrete overlays, Int. J. Pav. Eng. 11(6) (2010) 477-488.

[43] S.H. Song, G.H. Paulino, W.G. Buttlar, A bilinear cohesive zone model tailored for fracture of asphalt concrete considering rate effects in bulk materials, Eng. Fract. Mech. 73(18) (2006) 2829-2848.

[44] L.L. Mishnaevsky, Three-dimensional numerical testing of microstructures of particle reinforced composites, Acta Mater. 52(14) (2004) 4177-4188.

[45] P. Szewezyk, P. Hajela, Damage detection in structures based on feature - sensitive neural networks, J. Comp. Civ. Eng. 8(2) (1994) 163-178.

[46] X. Wu, J. Gahboussi, J.H. Garrett, Use of neural networks in detection of structural damage, Comput. Struct. 42(4) (1992) 649-659.

[47] S.F. Masri, A.G. Chassiakos, T.K. Caughey, Identification of nonlinear dynamic systems using neural networks, J. Appl. Mech. Trans. 60 (1993) 123-133.

[48] M.F. Elkordy, K.C. Chang, G.C. Lee, Neural networks trained by analytically simulated damage states, J. Comput. Civil Eng. 7(2) (1993) 130-145.

[49] J. Zhao, J.N. Ivan, J.T. DeWolf, Structural Damage Detection Using Artificial Neural Networks, J. Infrastruct. Syst. 4(3) (1998) 0093-0101.

[50] B. Yan, A. Miyamoto, Application of probabilistic neural network and static test data to the classification of bridge damage patterns, Smart Struct. Mater. Int. Soc. Optics Phot. (2003) 606-617.

[51] D. Specht, Probabilistic Neural Networks, Neural Networks. 3(1) (1990) 109-118.

[52] A.T.C. Goh, Probabilistic neural network for evaluating seismic liquefaction potential, Can. Geotech. J. 39(1) (2002) 219-232.

[53] H. Adeli, A. Panakkat, A probabilistic neural network for earthquake magnitude prediction, Neural Networks. 22(7) (2009) 1018-1024.

[54] R.O. Duda, P.E. Hart, D.G. Stork, Pattern Classification and Scene Analysis, second ed., New York: John Wiley &, Sons, 2000.

[55] K.Z. Mao, K.C. Tan, W. Ser, Probabilistic neural-network structure determination for pattern classification, EEE Trans. Neural Networks. 11(4) (2000) 1009-1016.

[56] D. Zongker, A. Jain, Algorithms for feature selection: An evaluation, In Pattern Recognition. Proc. 13th Int. Conf. 2 (1996) 18-22.

[57] MathWorks, MATLAB the language of technical computing, Version R2016a, MathWorks Inc., Natick, MA, USA, 2016.

[58] D.W. Aha, R. L. Bankert, A comparative evaluation of sequential feature selection algorithms, In Learning from Data. (1996) 199-206. Springer New York.

[59] J. Weston, S. Mukherjee, O. Chapelle, M. Pontil, T. Poggio, V. Vapnik, Feature selection for SVMs, In Proceedings of the 13th International Conference on Neural Information Processing Systems. (2000) 647-653. MIT Press.

[60] T. Haukaas, P. Gardoni, Model Uncertainty in Finite-Element Analysis: Bayesian Finite Elements, J. Eng. Mech. 137(8) (2011) 519-526.